Resource

Structure

A Multi-model Approach to Assessing Local and Global Cryo-EM Map Quality

Graphical Abstract

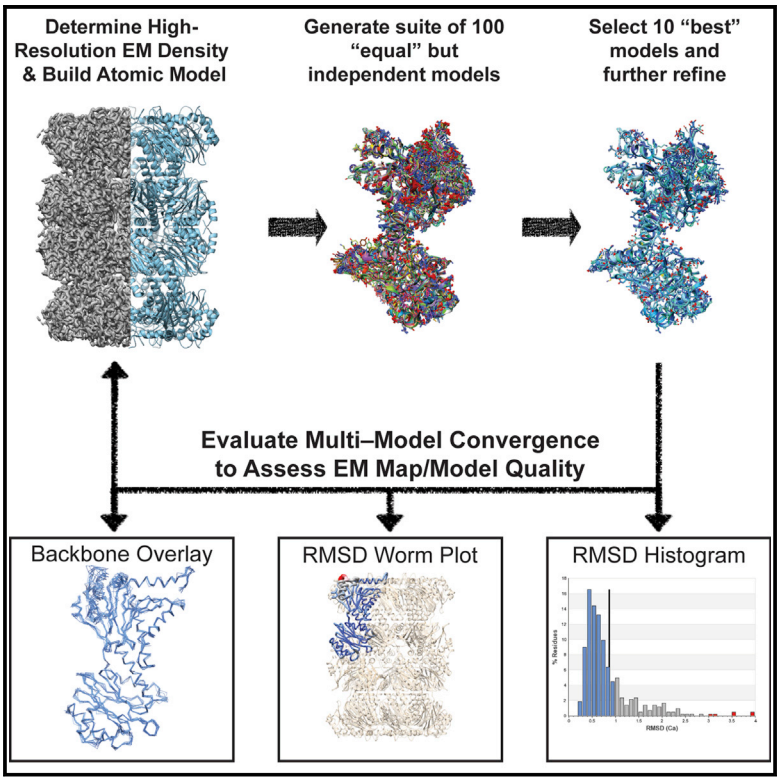

Authors

Mark A. Herzik, Jr., James S. Fraser, Gabriel C. Lander

Correspondence

glander@scripps.edu

In Brief

Herzik et al. present a user-independent pipeline for generating a suite of atomic models that represents an EM density better than a single atomic model. By measuring the agreement of these models, they provide a means to qualitatively and quantitatively assess EM map quality.

Highlights

- FSC-independent assessment of local and global EM map quality
- Multiple models describe conformational variability of an EM map
- Multi-model pipeline uses freely available software, assessed over 300 EMDB entries
- Generated a standardized suite of EM maps at a range of resolutions < 5Å

Herzik et al., 2019, Structure *27*, 344–358
February 5, 2019
https://doi.org/10.1016/j.str.2018.10.003

CellPress

CellPress

Structure
Resource

A Multi-model Approach to Assessing Local and Global Cryo-EM Map Quality

Mark A. Herzik, Jr.,[1] James S. Fraser,[2] and Gabriel C. Lander[1,3,*]
[1]Department of Integrative Structural and Computational Biology, The Scripps Research Institute, La Jolla, CA 92037, USA
[2]Department of Bioengineering and Therapeutic Science and California Institute for Quantitative Biology, University of California, San Francisco, San Francisco, CA, USA
[3]Lead Contact
*Correspondence: glander@scripps.edu
https://doi.org/10.1016/j.str.2018.10.003

SUMMARY

There does not currently exist a standardized indicator of how well cryo-EM-derived models represent the density from which they were generated. We present a straightforward methodology that utilizes freely available tools to generate a suite of independent models and to evaluate their convergence in an EM density. These analyses provide both a quantitative and qualitative assessment of the precision of the models and their representation of the density, respectively, while concurrently providing a platform for assessing both global and local EM map quality. We further use standardized datasets to provide an expected deviation within a suite of models refined against EM maps reported to be at 5 Å resolution or better. Associating multiple atomic models with a deposited EM map provides a rapid and accessible reporter of convergence, a strong indicator of highly resolved molecular detail, and is an important step toward an FSC-independent assessment of map and model quality.

INTRODUCTION

A molecular-level description of a macromolecule's conformational landscape is critical to understanding its role in a cellular context (Smock and Gierasch, 2009; Alberts, 1998; Frauenfelder et al., 1991; McCammon et al., 1977). Cryo-electron microscopy (cryo-EM) is an increasingly powerful structural technique for studying conformationally or compositionally heterogeneous macromolecules. Both types of heterogeneity are preserved upon vitrification during cryo-EM sample generation and can be discerned structurally using "*in silico* purification" that leverages sophisticated 2D and 3D classification and refinement protocols to identify homogeneous species (Nogales and Scheres, 2015; Sigworth, 2007). Indeed, a single data collection often yields several conformationally (Abeyrathne et al., 2016; Bai et al., 2015; Banerjee et al., 2016; He et al., 2016; Zhou et al., 2015) or compositionally distinct structures (Davis et al., 2016; Shen et al., 2015; Tsai et al., 2017). Although image-processing strategies typically strive to identify the most homogeneous particles within a dataset, cryo-EM reconstructions frequently possess large internal variations in resolution (Cardone et al., 2013). This variability in resolution presumably results from residual structural heterogeneity (encompassing both compositional and conformational) and imperfect particle alignment during the reconstruction.

Despite local resolution variation, a single, static atomic model is typically used to represent these structures, an approach inherited from the X-ray crystallography community. As such, a single-conformer model with uncertainty modeled by an isotropic Gaussian distribution of the position of each atom (atomic displacement parameter, or B factor) is presented. The B factor is an incomplete description of the extent of heterogeneity exhibited by a structure because isotropic motion is a poor approximation for most protein conformational heterogeneity and it additionally convolves uncertainty, model error, and refinement restraints (Kuriyan et al., 1986; Kuzmanic et al., 2014). The local accuracy and precision a single static model cannot be evaluated by any single metric, forcing users to examine a combination of B factors, improbable geometric outliers, and local correlation to the density (X-ray or EM) as a means to assess model quality. However, the relationship between the atomic model and the experimental data differ greatly between X-ray crystallography and EM. Whereas atomic models derived from X-ray diffraction are inextricably linked to the data because iterative improvements in phase information arise from an improved atomic model, EM density maps are generated independently of an atomic model. Because the target EM density should typically remain unchanged during atomic model generation and refinement, the question of how well a model converges is less subject to model bias and primarily reflects the local resolution/quality of the map.

Many alternative representations of macromolecular structure have been proposed to overcome the limitations of using a single conformer and B factors (reviewed in Woldeyes et al. (2014)). In X-ray crystallography, these alternative representations can be grouped into two different classes: (1) an ensemble of multiple complete models that each are presented as *independent* but equally valid interpretations of the structural data (DePristo et al., 2004), and (2) ensembles of multiple conformations that are presented as a *collective* interpretation of the structural data (Burnley et al., 2012; Keedy et al., 2015a; Levin et al., 2007). These methods are similar to the current practices for generating NMR ensembles that are either equally valid interpretations of restraints (Wuthrich, 1990) or that use more

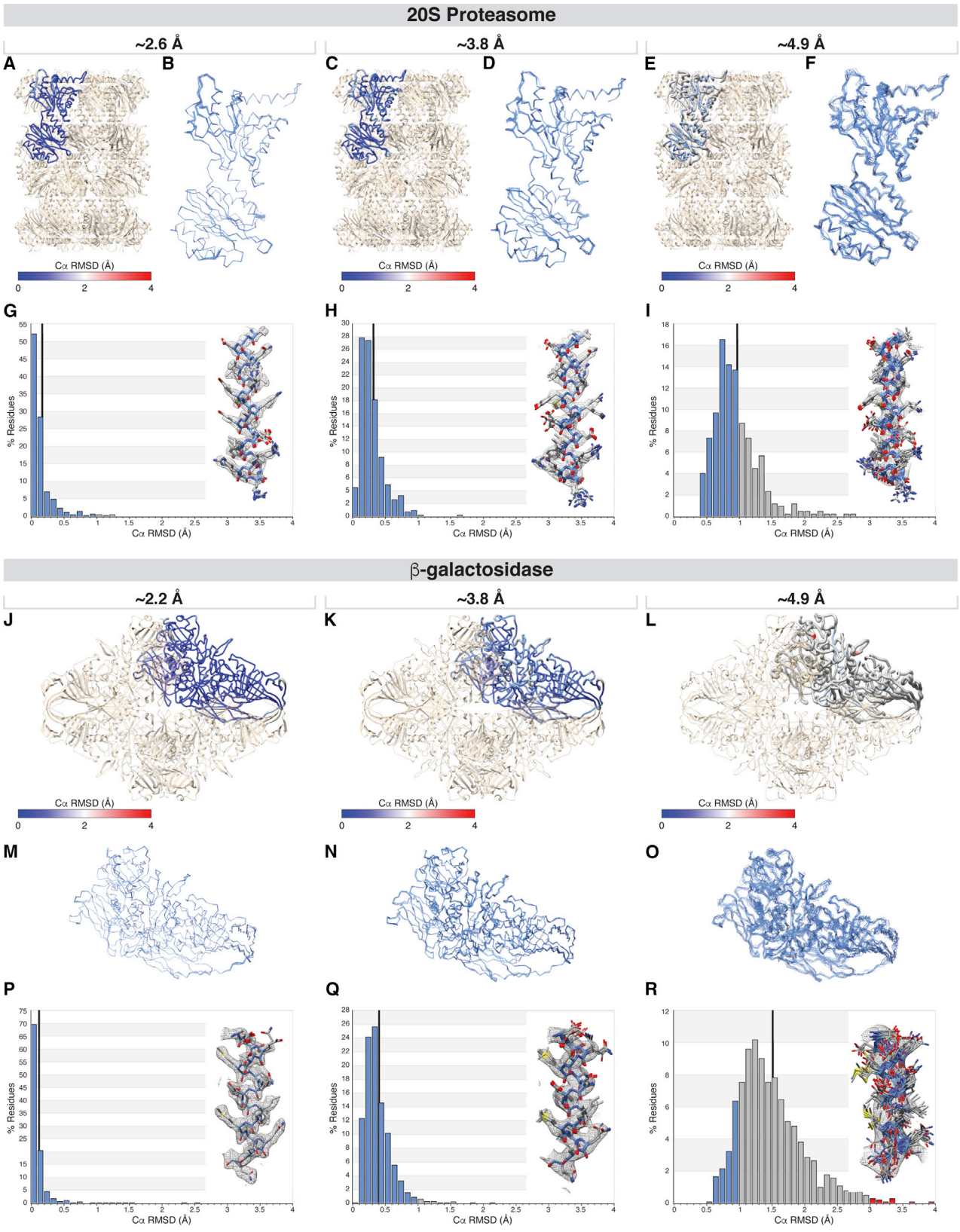

(legend on next page)

sophisticated averaging schemes (Lange et al., 2008), both of which are routinely deposited at the Protein Data Bank (www.rcsb.org) (Berman et al., 2000). The conformational heterogeneity represented by these ensembles arises not only from the dynamic nature of the macromolecule, but also from uncertainties in image processing and model generation/refinement. While the collective ensembles can, in principle, accurately capture discretely conformations observable at high resolution (Singharoy et al., 2016), the independent ensembles are biased toward the most populated conformation and therefore yield an estimate of precision (Terwilliger et al., 2007); however, both model types demonstrate the limitations of the single static model and the inadequacy of the B-factor approximation to model the underlying conformational heterogeneity (Kuzmanic et al., 2014).

Despite proposals advocating alternative representations in X-ray crystallography (Furnham et al., 2006), the practice has not been widely adopted. However, because independent models provide a reasonable local estimate of the lower bound of model precision and do not introduce additional parameters (Terwilliger et al., 2007), they may offer additional utility in addressing an emerging challenge in EM: evaluating local map quality and the uncertainty of the model. This issue emerges because EM lacks foolproof and robust measures of local and global resolution primarily relying on the "gold-standard" Fourier Shell Correlation (FSC) (Henderson et al., 2012; Scheres and Chen, 2012). The FSC reports on the resolution of a determined structure by measuring the correlation across spatial frequencies between two independently refined "half-maps" (Henderson et al., 2012; Penczek, 2010; Saxton and Baumeister, 1982; Scheres and Chen, 2012; van Heel and Harauz, 1986), a measure of the self-consistency of the data rather than a true measure of "resolution." There are a variety of ways in which the global resolution can be overestimated, such as by excluding poorly resolved regions from calculation of the FSC through application of a 3D mask. Furthermore, reconstructions with preferred orientation can contain extensive anisotropy in resolution that will not be evident in the FSC curve (Lander et al., 2013; Naydenova and Russo, 2017; Penczek, 2002; Tan et al., 2017; Urnavicius et al., 2015). This problem is further compounded when a single value from this curve is ascribed to an EM structure, providing only an approximation of the quality of the molecular details contained within a reconstruction, and without indication of the degree of resolution variation. As a result, care must be taken when evaluating a map solely on the FSC-reported resolution values (see Subramaniam et al. (2016) and Neumann et al. (2018) for further discussions on the limitations of FSC).

Here we show that the generation of multiple independent atomic models using an EM density and subsequent analysis of their atomistic agreement statistics provide model quality metrics that directly correlate with global and local EM map quality. Importantly, this multi-model approach provides both a quantitative and qualitative assessment of the precision of the models and their representation of the density, respectively. We further show that this analysis can be applied to most EM maps reported to be at 5 Å resolution or better, and use standardized *in silico* datasets to provide an expected multi-model agreement criterion for EM maps across a broad resolution range. Although the methodology presented here aims to report on the quality of the cryo-EM density into which a model has been built, not the accuracy of the model itself, it is important to note that the method is sensitive to the quality of the model which seeds the rebuilding and refinement procedure.

RESULTS

Resolution Devolution: Generating Lower Resolution Structures *In Silico* from High-Resolution Cryo-EM Data

To establish a quantitative baseline correlation between the precision of an atomic ensemble and the resolution of an EM density, we first generated a standardized set of EM structures using previously published datasets. Electron Microscopy Public Image Archive (EMPIAR) (Iudin et al., 2016) datasets 10025 (20S proteasome) (Campbell et al., 2015) and 10061 (β-galactosidase) (Bartesaghi et al., 2015) were preprocessed using the Appion processing environment (Lander et al., 2009), and refined using RELION (Scheres, 2012) to ~2.7 Å and ~2.2 Å resolution, respectively (see STAR Methods, Figure 1, Data S1). To generate lower resolution structures from these datasets, a random translational offset within a defined range was applied to the refined particle coordinates (see STAR Methods). The degree of random translational offset was adjusted empirically for each dataset to ultimately yield 14 structures of the 20S proteasome from ~2.7 Å to ~4.9 Å resolution and 14 structures of β-galactosidase from ~2.2 Å to ~4.9 Å resolution.

A comparison of these "simulated" lower resolution maps with previously published reconstructions at corresponding resolutions, i.e., 20S proteasome structures at ~3.3 Å and ~4.8 Å resolution (EMD-5623 [Li et al., 2013] and EMD-6219 [Wang et al., 2015], respectively) and β-galactosidase at ~3.2 Å resolution (EMD-5995 [Bartesaghi et al., 2014]), show comparable quality of density and FSC curves (Data S2). The asymmetric unit (ASU) from each of the generated lower resolution 20S proteasome and β-galactosidase structures is shown in Data S3, respectively. Comparison of these densities shows a gradual but noticeable decline in resolvable side chain and backbone features, as anticipated (Data S3). Together, these comparisons

Figure 1. 20S Proteasome and β-Galactosidase RMSD (Cα) Analysis across Various Resolutions

The results of the multi-model pipeline and corresponding root-mean-square-deviation (RMSD) (Cα) analysis are presented for the 20S proteasome core and β-galactosidase, each at three different resolutions: 20S proteasome at ~2.7 Å (A, B, and G), at ~3.3 Å (C, D, and H), and at ~4.9 Å (E, F, and I), and β-galactosidase at ~2.2 Å (J, M, and P), at ~3.3 Å (K, N, and Q), and at ~4.9 Å (L, O, and R). For each structure, the ASU is shown in worm representation and colored by per-residue RMSD value (A, C, E, J, K, and L). Line representation for the backbone atoms for the top 10 models of each ASU for each EM density are shown (B, D, F, M, N, and O). For each structure, a per-residue RMSD (Cα) histogram plot is displayed (G, H, I, P, Q, and R) where RMSDs less than 1 Å are shown in blue, RMSDs between 1 and 3 Å are shown in gray, and RMSDs greater than 3 Å are shown in red. The mean per-residue Cα RMSD value is shown as a black vertical bar. (G, H, and I insets) Residues 49–72 of the 20S proteasome β-subunit are shown in stick representation with the corresponding EM density (zoned 2 Å around models) shown as a gray mesh. (P, Q, and R insets) Residues 368–383 of β-galactosidase are shown in stick representation with the corresponding EM density (zone 2 Å around models) shown as a gray mesh. For all stick representations, backbone atoms are colored blue with side chain atoms shown in dark gray.

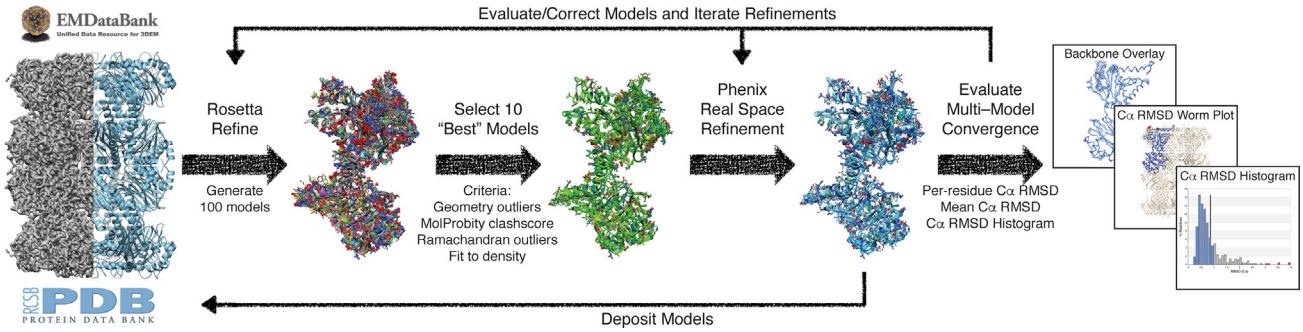

Figure 2. Overview of the Multi-model "Pipeline"

For each EMDB entry, the corresponding PDB entry was "cleaned" (see STAR Methods) and was then refined against the primary EMDB map entry using Rosetta with a desired output of 100 models. The statistically "best" 10 models were then subjected to real-space refinement in Phenix. The per-residue RMSD (Cα) was then calculated for each model against the refined structures. Thick arrows indicate the linear pipeline employed in this study, while the thin arrows represent the iterative process that could be utilized by a general user to generate a previously unpublished structure.

corroborate the quality of the multi-resolution suite of maps generated in this study.

User-independent Pipeline to Generate Multiple Atomic Models Using Cryo-EM Maps

Initial models for refinement using Rosetta were generated by stripping the associated PDB files (PDB: 1YAR [Forster et al., 2005] and 5A1A [Bartesaghi et al., 2015] for 20S proteasome and β-galactosidase, respectively) of cofactors, removing alternate conformations, setting all occupancies to one, resetting all B factors, and correcting Ramachandran and geometric outliers. These initial models were refined into the EM density using the corresponding symmetry and resolution values while adjusting the Rosetta weighting and scoring functions according to the estimated map resolution (Wang et al., 2016). To sample a large conformational space for each given map, regardless of resolution, 100 models were generated using Rosetta (Figure 2). A comparison of the top 10 structures resulting from 100 or 1,000 Rosetta-generated models using ~2.8 Å and ~4.8 Å resolution densities were essentially indistinguishable (see Figure S1), indicating that 100 models sufficiently sample the conformational space constrained by the EM density for these convergence analyses. Notably, this sampling of conformational space could also be achieved using other methodologies that effectively perturb the initial model, such as simulated annealing.

The 100 models were then ranked based on the number of Ramachandran outliers, geometry violations, Rosetta aggregate score, and MolProbity clashscore (Chen et al., 2010). These combined criteria were chosen as they provide a quantitative assessment of a model's geometry as well as its agreement with the cryo-EM density. The ten structures that consistently scored the best across all the above mentioned categories were selected for real-space refinement using Phenix (Adams et al., 2010) using the developer-recommended geometry parameters and the estimated map resolution for weighting. Real-space refinement of coordinates and B factors was performed because the resulting structures from Phenix generally yielded better geometries and model-map correlation coefficients than the Rosetta models. However, algorithm and parameterization improvements in recent and future releases of Rosetta may remove the need for this additional refinement step (Wang et al., 2016). As evidence of a lack of starting model bias, we show that a β-galactosidase loop was rebuilt correctly from an incorrect initial model (Figure S2).

Following real-space refinement using the Phenix suite, the per-residue CαRMSD, or C3′-C4′ RMSD for nucleic-acid-containing structures, was calculated for all residues in the asymmetric unit of the refined structures (Figures 1 and 2). The all-atom RMSD values were also calculated, with these values typically greater than Cα (or C3′-C4′) RMSD values by ~1–1.5 Å (data not shown). In total, 10 models were used to derive validation statistics for all densities in this testing suite, providing a measure of unity in atomistic positions within the asymmetric unit relative to reported resolution. To provide a general overview of the atomic convergence of each structure, the mean RMSD value and a RMSD histogram were also calculated for each map (Figure 1, Data S4).

Multi-model Agreement Provides Global and Per-residue Metrics for Assessing Cryo-EM Map Quality

The multi-model agreement statistics directly correlate with map resolution, with the mean RMSD of each group of models increasing as the resolution of the map worsens from ~2.2 Å to ~4.9 Å (Figure 1, Data S4). For example, the mean RMSD value increases gradually from 0.30 Å for the ~2.7 Å resolution 20S proteasome dataset, to 0.36 Å and 1.14 Å for the ~3.8 and ~4.9 Å resolution datasets, respectively (Figures 1G–1I, and Data S4A). A similar trend is also observed for the β-galactosidase datasets, with the mean RMSD increasing from 0.25 Å to 1.76 Å as the resolution of the map decreases from ~2.2 Å to ~4.9 Å resolution, respectively (Figures 1P–1R, and Data S4B). Lower resolution maps possess fewer well-resolved features for accurate placement of side chain atoms and, in some cases, are completely absent of side chain densities (Data S3). Furthermore, EM maps reported to worse than ~5 Å resolution often contain secondary structure elements that are nearly feature-less, leading to ambiguous β-strand or α helix register (Hryc et al., 2011). In agreement with these observations, comparison of the same α helix from the "best" 10 models and corresponding EM density from each of the 20S proteasome and β-galactosidase structures reveals decreasing multi-model agreement as the resolution of the map worsens (Figure 1).

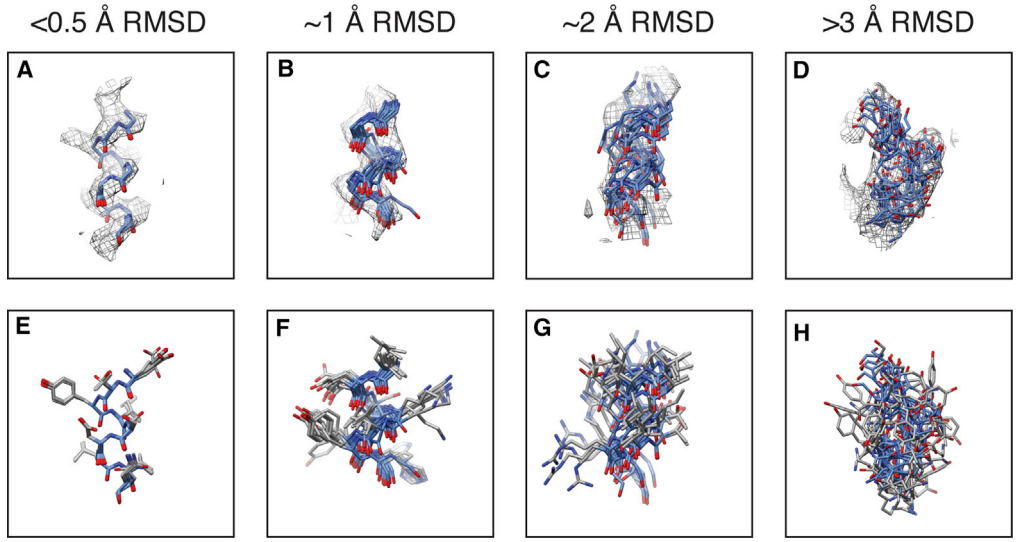

Figure 3. Multi-model Convergence for Given Cα RMSD Values

(A–D) The backbone atoms from the top 10 models corresponding to RMSD values of <0.5 Å (A), ~1 Å (B), ~2 Å (C), and >3 Å (D) are displayed with corresponding EM density (zoned 4 Å around displayed atoms).

(E–H) The same residues displayed in panels (A–D) are displayed in panels (E–H), respectively, with side chain atoms shown. For all stick representations, backbone atoms are colored blue with side chain atoms shown in gray.

Specifically, the pronounced side chain densities that gives rise to near perfect multi-model agreement for the highest resolution structures (Figures 1G and 1P) are diminished in the lower resolution structures (Figures 1I and 1R), corresponding to increased heterogeneity in backbone and side chain atom placements (i.e., increased mean and per-residue RMSDs), correlated with worsening map resolution. As evidenced in Figure 3, regions of the model exhibiting $\geq$3 Å per-residue RMSD values can show shifts in amino acid sequence register.

Although EM densities are ascribed a single resolution value, the local resolution is never isotropic across the entire map, with most structures exhibiting a marked range of varying local resolution (Adams et al., 2010; Cardone et al., 2013; Leschziner and Nogales, 2007). Even the 20S proteasome from the thermophilic bacterium *Thermoplasma acidophilum*, which possesses high internal symmetry (D7) and high thermal stability (thermoinactivation ~97°C) (Beadell and Clark, 2001), displays a range of local resolution and thus varying map quality (Figure 4 and Data S4A). Due to the direct correlation between multi-model agreement and EM density quality (*vida supra*), we reasoned that examination of the multi-model agreement statistics at a per-residue level would inform on the local map quality (Figures 1A, 1C, 1E, and 1J–1L). Each structure is represented using a tricolor heatmap coloring scheme with residues exhibiting Cα RMSDs less than 1 Å colored blue, between 1 and 3 Å colored gray, and greater than 3 Å colored red. For all 20S proteasome and β-galactosidase datasets, the regions exhibiting the most heterogeneity (highest per-residue Cα RMSD values) are localized to the regions least well resolved, as evidenced by the poorer EM density and lower local resolution estimates (Figures 1 and 4, Data S4).

The RMSD histogram provides an easily interpretable means to quickly evaluate both the overall quality of an EM map, as well as informing on the range of resolutions contained within the map. An overall shift of RMSD histogram to the right, where the mean and mode of the RMSD values are similar, is indicative of a general worsening in map resolution, exemplified by an increasing number of residues possessing greater than 1 Å RMSD values (Figures 1G–1I and 1P–1R, Data S4). However, a pronounced right-skewness of the per-residue RMSD histogram, where the mean and mode diverge, is indicative of a map that contains a wide range of local resolutions (Figure 4). Examination of EMD-6479 (Dambacher et al., 2016) corroborates the observation that per-residue RMSD values inform on local map quality, exhibiting a pronounced decrease in local resolution at the periphery of the molecule, with the core resolved to ~3.2 Å resolution, while the outer, peripheral regions are resolved to ~5 Å resolution or worse. Accordingly, the gradual decrease in local resolution as densities extend toward the periphery of the molecule is consistent with a gradual increase in the per-residue Cα RMSD values, and a substantial right-skewness of the Cα RMSD histogram (Figure 4). Together, these analyses indicate that both the mean RMSD and profile of the Cα RMSD histogram provide a means to globally assess the multi-model agreement and, presumably, overall map quality, with per-residue Cα RMSD values reporting on local map quality.

Comparison of the per-residue RMSD values and the B factors assigned from Phenix real-space refinement shows a correlated trend of values, with the highest values reported at peripheral and flexible regions (Figure S3). However, estimation of B factor is not consistent from one refinement package to another, and refinement strategies and parameters can influence the B-factor values even when using a single package. This can result in a wider range of variability in B-factor values than RMSD values when comparing one structure with another, complicating comparisons of density quality between depositions. Furthermore, B-factor values considered to be extremely "high" by crystallographic standards (300–400), imply an RMSD of ~3.5 Å

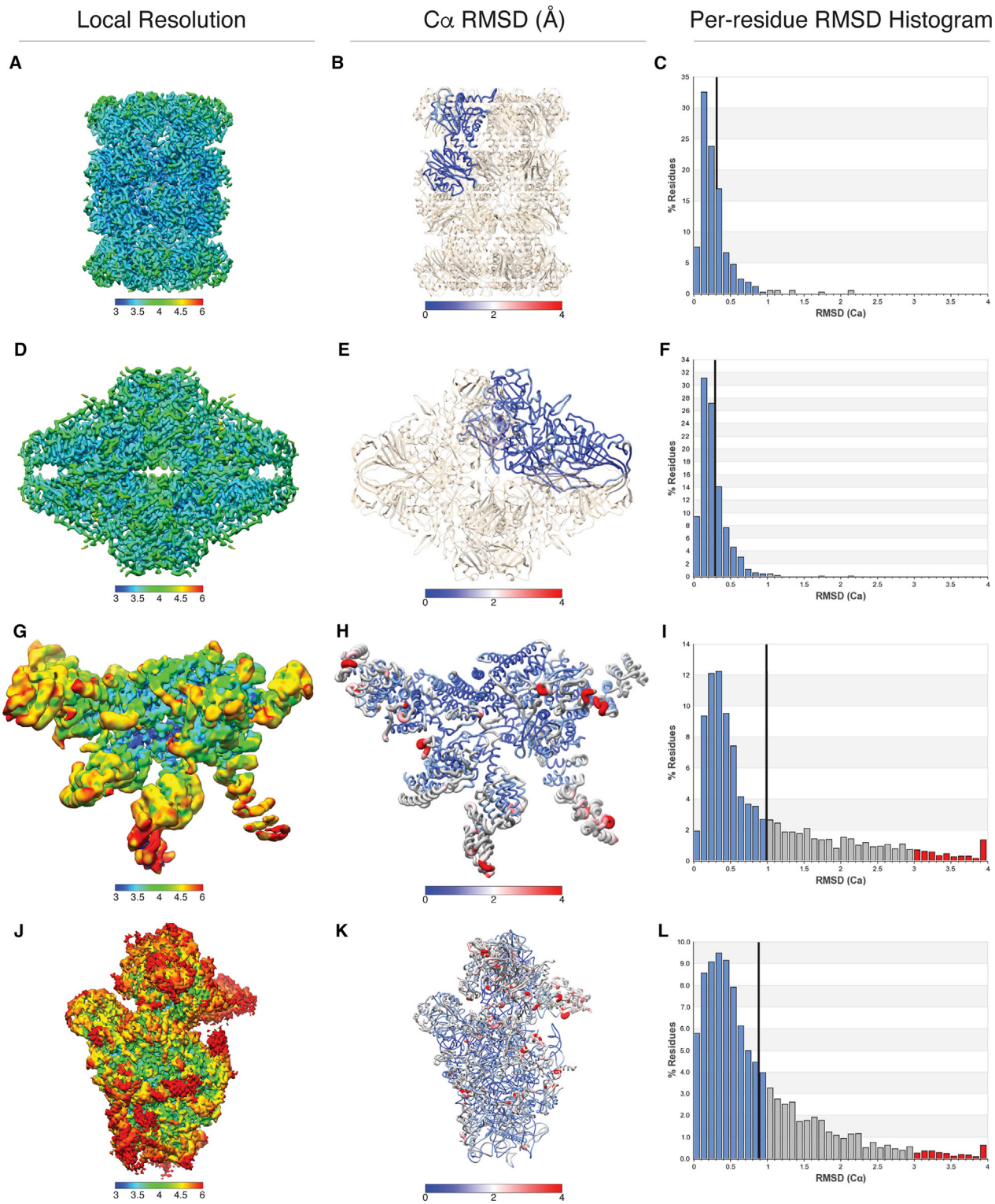

Figure 4. Influence of Map Resolution Variance on Convergence of Atomic Models

Three-dimensional local resolution plots for EM maps of 20S proteasome (A), β-galactosidase (D), EMD–6479 (G), and EMD–2764 (J) having overall FSC-reported resolutions of ~3.5 Å (EMD-2764 is reported to be 3.75 Å). A worm plot and histogram of the per-residue RMSDs (B, E, H, and K, and C, F, I, and L, respectively) are shown for each map. The worm plots show that areas exhibiting increased per-residue RMSDs are correlated with lower local resolution estimates, as expected. The histograms show that as the range of resolutions contained within a map increases, the right-skewness of the histogram also increases along with the separation of the mean (black line) and mode of the histogram.

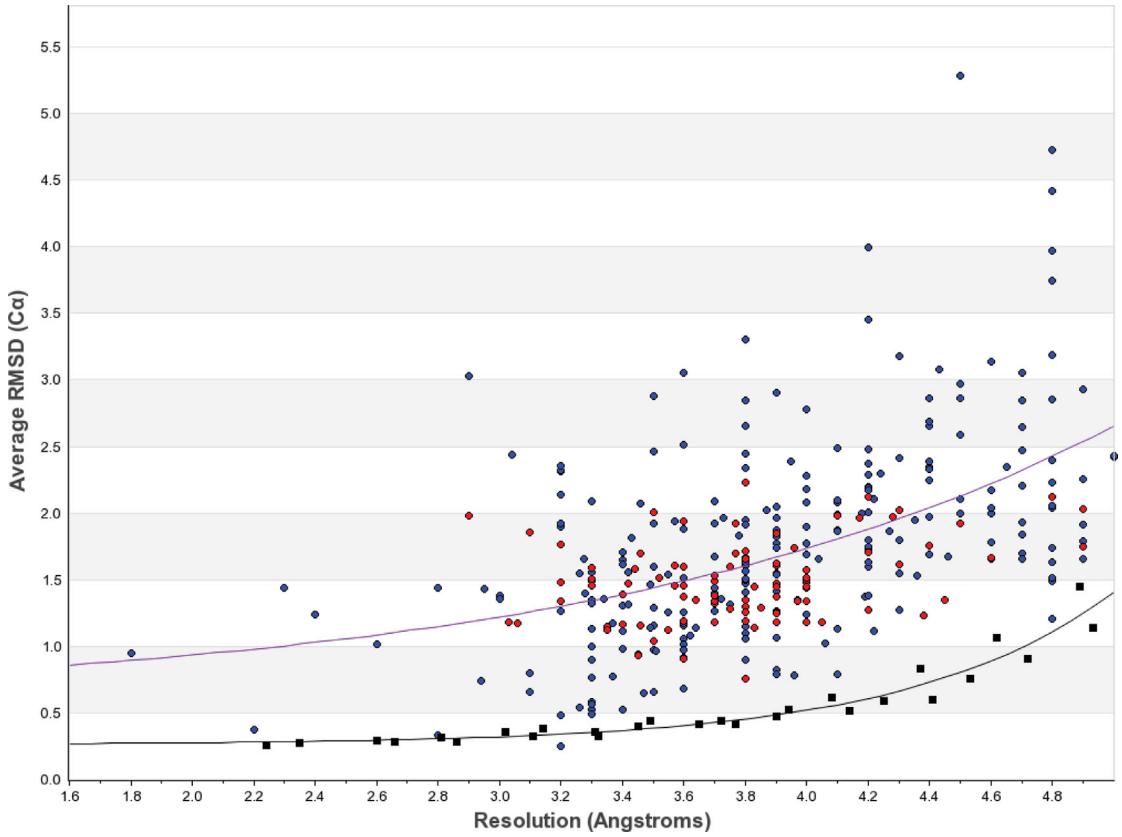

Figure 5. Average Per-residue RMSD versus FSC-Reported Resolution

The average per-residue RMSD value calculated from the "best" 10 models resulting from the multi-model pipeline plotted versus the FSC-reported resolution of the target map. Values for EMDB entries are shown as either blue circles (protein-only entries) or red circles (nucleic acid-containing entries) and values for the *in silico* datasets are shown as black squares. The black line is a non-linear regression fit against the 20S and β-galactosidase structures generated in this study. The purple line is a non-linear regression fit against the EMDB entries.

(Kuzmanic et al., 2014), which, as demonstrated by the RMSD histograms (Figure 4I), is an overestimation of the electron density quality present in cryo-EM structures. An RMSD of 4 Å would correspond to a B factor of over 400, which is higher than observed in most refinements, reflecting the inappropriateness of the isotropic approximation of microscopic heterogeneity (Kuriyan et al., 1986; Kuzmanic et al., 2014), which can potentially be modeled better by ensemble or multi-conformer approaches (Woldeyes et al., 2014). In contrast, assignment of a per-residue RMSD provides a consistent and interpretable reporter on the quality of EM density.

Evaluation of the Electron Microscopy Data Bank Using the User-independent Multi-model Pipeline

We assessed all Electron Microscopy Data Bank (EMDB, www.emdatabank.org) depositions having a reported resolution of better than 5 Å with an associated PDB entry (see STAR Methods and Figure 2). As in the simulated data (Figure 1, Data S4), a scatterplot of the experimental multi-model agreement statistics (mean Cα RMSD for polypeptide, C3′-C4′ for nucleic acid) for all 312 structures analyzed in this study against their reported resolution value shows a strong correlation, with higher mean RMSD values associated with lower resolution structures (Figure 5). Specifically, plotting RMSD versus resolution yields an exponential fit against the data with the point of maximum curvature located at ~4.1Å, for both the EMDB and *in silico* datasets (Figure 5). These observations indicate that beyond ~4.1 Å resolution, where clearly resolvable side chain density becomes rare, convergence of multiple models against the density decreases precipitously (Figure 5). The observation that both the 20S and β-galactosidase datasets, while exhibiting the same general trend as the cumulative EMDB entries, consistently present a ~1.5 Å lower overall RMSD, is both a result of the limited structural heterogeneity/flexibility in the maps and the high quality of the initial atomic models (high-resolution X-ray model for 20S PDB: 1YAR [Forster et al., 2005] and β-galactosidase PDB: 1DP0 [Juers et al., 2000]). As a result, the structures are initialized at a lower global minimum than what would typically be obtained for most models built *de novo* into cryo-EM densities at 3.5 Å resolution or worse.

A non-linear regression fit of mean RMSD values versus resolution provides an estimated mean RMSD value for models refined against an EM density for various reported resolutions between ~2 and 5 Å resolution (Figure 5). As a result, structures giving rise to mean RMSD values that lie substantially above the regression line are likely to possess EM density that is worse than anticipated, given the FSC-reported resolution. Whether the density is poorer than expected for the given resolution, or if

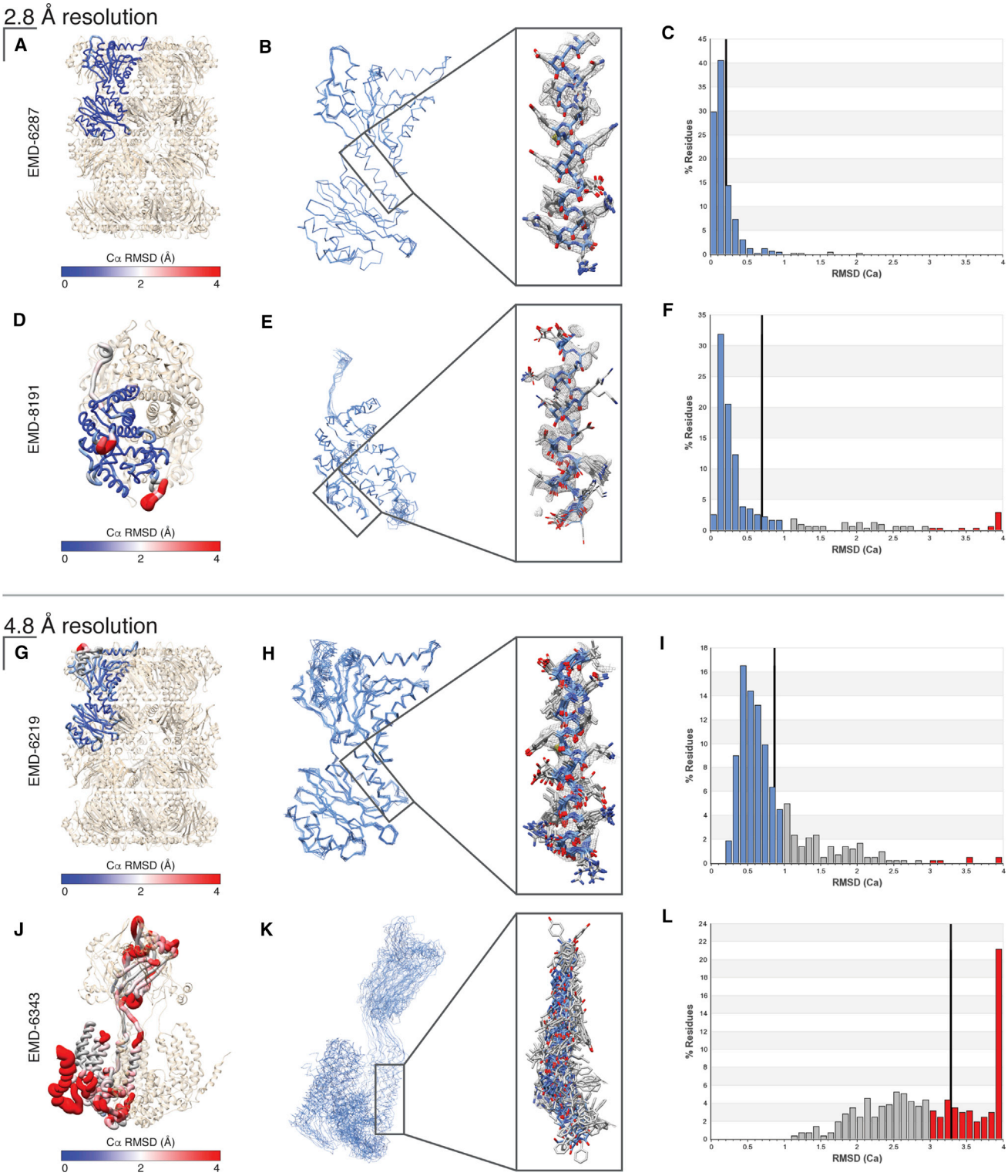

Figure 6. Variation in Map Quality at Similar FSC-Reported Resolution Values: Comparisons of Maps at 2.8 Å and 4.8 Å Resolution

Comparison of the multi-model analysis for structures at 2.8 Å resolution – EMD-6287 (A–C) and EMD-8191 (D–F) – and at 4.8 Å resolution – EMD-6219 (G–I) and EMD-6343 (J–L). For each structure (left), the ASU is shown in ribbon representation with each residue colored by the per-residue RMSD (Cα) value (the rest of the

(legend continued on next page)

the reconstruction contains large local resolution variations, can be assessed by examining the per-residue RMSDs and RMSD histogram for the entry (Figures 1 and 4, Data S4). These elevated RMSD values may also be due to modeling errors introduced by the user-independent, automated pipeline.

It is apparent from this plot that most structures (72%) worse than ~4.5 Å resolution have a mean RMSD value of 2.0 Å or above by our analyses. Such RMSD values arise from significant backbone displacements between models, often with little agreement in side chain placement. Regardless of resolution, maps giving rise to a mean RMSD of greater than 3 Å show significant heterogeneity in backbone atomic coordinates, with almost no agreement in side chain placement for a majority of the map. Great caution and consideration should be exercised in the interpretation of such models. In contrast, some maps with a reported resolution of worse than 4.0 Å resolution yielded mean RMSDs that were lower than 2 Å (EMD-8188, EMD-3180), suggesting an adequate degree of confidence in the agreement between models and thus, the approximate placement of atoms in much of the map.

Not All Maps Are Created Equally: Case Studies at 2.8 Å and 4.8 Å Resolution

To report on the variations in the quality of EM density for maps that are reported to have identical resolutions, we focused our multi-model agreement analyses on EMDB entries reported at ~2.8 Å and ~4.8 Å resolution (Figure 6). EMDB entries 6287 (Campbell et al., 2015) and 8191 (Merk et al., 2016) were both reportedly determined to ~2.8 Å by FSC. Our analyses, as expected, yielded a suite of models for these two entries with mean RMSD values <1 Å (0.33 and 0.69 Å, respectively). EMDB entry 8191 shows a larger variation in local map quality, with several loops and secondary structure elements at the periphery more poorly resolved than the core of the molecule. As a result, the per-residue Cα RMSD values in these regions are elevated above the mean, as evidenced by the following: more gray and red regions when coloring each residue by the per-residue Cα RMSD value (Figure 6D); by increased heterogeneity in the atomic coordinates across the "best" models (Figure 6E); and by the right-skewed histogram (Figure 6F). In contrast, EMDB entry 6287 shows little variation in local map quality and, as a result, yields a narrow RMSD histogram with only ~3% of residues with Cα RMSDs greater than 1 Å (Figures 6A and 6C). By comparison, EMDB entry 8191 yields ~10% of residues with per-residue Cα RMSD values greater than 1 Å (Figure 6F). In addition, comparison of extracted regions from both EM maps (zoned 2 Å around an α helix with an approximate mean RMSD as the entire molecule) indicate that EMDB entry 8191 has a lower percentage of well-resolved side chain densities, as well as broader backbone density as compared with EMDB entry 6287 (Figures 6B and 6E).

The variations in map quality that give rise to large discrepancies in multi-model agreement become much more pronounced for structures reported at resolutions worse than ~4 Å. An example of this is demonstrated by our analyses of EMDB entries 6219 (Wang et al., 2015) and 6343 (Ge et al., 2015), both at a reported resolution of ~4.8 Å. Analysis of EMDB entry 6219 shows high multi-model agreement for most of the ASU, with a majority of the ASU possessing per-residue Cα RMSDs less than 1 Å (Figure 6I). There are several poorly resolved densities at the periphery of EMD-6219, which give rise to elevated RMSDs, shown in red (Figures 6G and 6I). However, a majority of the map possesses well-resolved backbone density, allowing for consistent placement of backbone atoms (Figure 6H). In contrast, analysis of EMDB entry 6343, which is also reportedly resolved to ~4.8 Å resolution, shows predominantly elevated per-residue Cα RMSDs, with a mean RMSD value of 3.9 Å, with no residues better than 1 Å Cα RMSD. Over 48% of the residues yielded Cα RMSD values greater than 3 Å (Figures 6J and 6L). Examination of the EM density around an α helix (with an approximate mean RMSD of the entire molecule, middle panel) located adjacent to the symmetry axis contains little-to-no discernable side chain density (Figure 6K). As a result, the backbone atoms vary significantly across the models, with some helices distant from the 3-fold symmetry axis showing significant translation of the α helix backbone and/or complete changes in helical register.

Examination of EMDB Entry 3295

The 20S proteasome and β-galactosidase structures detailed above are highly symmetric and exhibit less variation in local resolution than most entries in the EMDB (Figure 4, Data S4). EMDB entry 3295 exemplifies a deposition reported to be at high resolution with an associated full atomic model (PDB: 5FTJ), but which also exhibits a wide range of local resolution in the map (Banerjee et al., 2016). The overall resolution of the map is reported to be 2.3 Å; however, unlike the 20S proteasome or β-galactosidase, the quality of the map exhibits extremely internal variability, with external loops and an entire peripheral domain that are poorly resolved (Figure 7).

EMD-3295 is a homohexamer containing a well-ordered hexamerization domain, as well as an N-terminal domain that extends from the core that is resolved to a much worse resolution than the reported ~2.3 Å resolution (Figure 7A). The disorder of this domain is clearly evident when one extracts the EM density within 2 Å radius of the atomic model of a single ASU (Figure 7B), shown as a cartoon in Figure 7C. The EM density and associated atomic model were subjected to the linear multi-model pipeline described above and, as anticipated, there is excellent multi-model agreement within the core of the protein, and lower levels of agreement in the poorly resolved N-terminal domain (Figure 7D). These observations are corroborated by the varied conformational heterogeneity across the resulting multiple models (Figure 7D), the per-residue Cα RMSD worm plot (Figure 7K, inset), and the pronounced right-skewness of the per-residue Cα RMSD histogram (Figure 7K). Furthermore,

molecule is colored in wheat). (Middle) The ASUs from the top 10 models are shown in line representation with a single α helix (inset, helix atoms exhibit approximately the mean Cα RMSD value for the entire molecule) and corresponding EM density (zoned 2 Å around atoms) shown in gray, and (right) the per-residue RMSD (Cα) histogram plot. For all stick representations, backbone atoms are colored blue with side chain atoms shown in gray. For the histograms, the average per-residue Cα RMSD is shown as a black vertical bar.

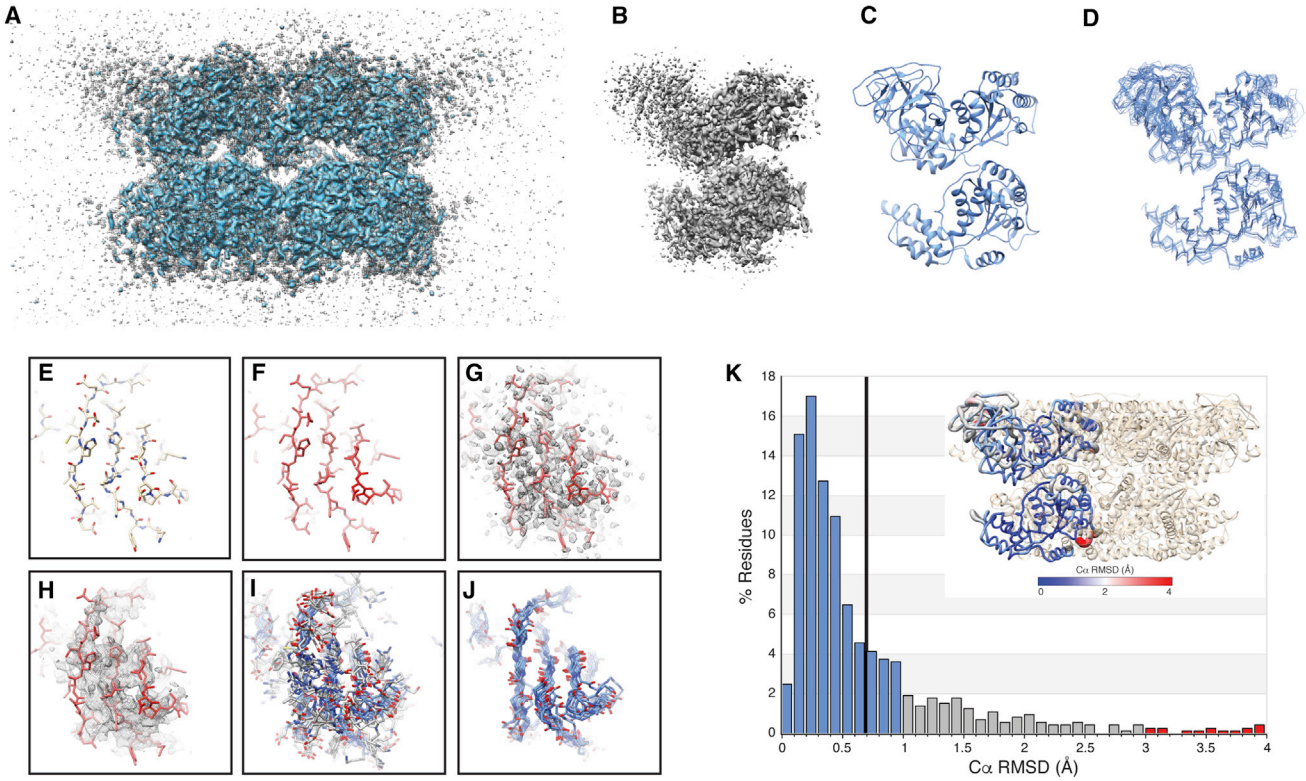

Figure 7. Case Study: EMD-3295

(A) The primary map for entry EMD-3295 displayed at two different contour levels: lower threshold (gray) and higher threshold (blue).

(B) Corresponding EM density from EMD-3295 for a single ASU (zoned 5 Å around chain A).

(C) Chain A from PDB: 5FTJ shown in ribbon representation.

(D–J) (D) Backbone atoms of chain A from the top 10 models generated by the multi-model pipeline shown in line representation. The same region of PDB: 5FTJ shown in stick representation (E), colored by Cα B factor (F), with the sharpened EM density from EMD-3295 shown as gray mesh (G), with the unsharpened EM density from EMD-3295 shown as gray mesh (H), the top 10 models from this study shown in stick representation (I), and only backbone atoms (J). For (I) and (J), the backbone atoms are colored blue with the side chain atoms shown in dark gray.

(K) Histogram plot of the per-residue RMSDs (Cα, RMSDs less than 1 Å shown in blue, RMSDs between 1 and 3 Å shown in gray, and RMSDs greater than 3 Å shown in red) with the ASU shown in ribbon representation and colored by per-residue RMSD (K, inset). For the histogram, the average per-residue Cα RMSD is shown as a black vertical bar.

comparison of the per-residue Cα RMSDs for this domain to the rest of the molecule (Figure 7K) shows that most of the disordered N-terminal domain have Cα RMSD values above the mean, with the highest Cα RMSD values localized almost entirely to the N-terminal domain and two peripheral loops.

The multi-model analysis of EMD-3295 clearly outlines the rationale for depositing multiple atomic models for cryo-EM densities. A ~2.3 Å resolution structure would be considered by the broad structural biology community to be of high quality, even in regions that are assigned high B factors. However, it would be imprudent to carry out a detailed interpretation of the deposited atomic coordinates within the N-terminal domain due to the extremely poor density in this domain. A naive user could examine the panels in Figure 7 and rapidly deduce that the N-terminal region of this map is poorly ordered and consider the low confidence of atom positioning when interpreting the model. Furthermore, if the same naive user is presented with ten or more atomic models upon downloading the PDB entry associated with cryo-EM map for the purposes of, for example, designing a mutagenesis experiment, the user would intuitively be able to distinguish between alternative interpretations embodied by the widely divergent models of poorly ordered regions and the converged high-confidence models for well-ordered regions.

Do Multiple Model Outputs Recapitulate the Variable Quality of Cryo-EM Density?

To assess how well the variability in the top 10 models represent the local variability in the EM target maps, several rounds of the multi-model pipeline were employed using a summed synthetic map as the target density for subsequent rounds. For example, the ten final models for the 20S reconstruction (at three different resolutions: ~2.6 Å, ~3.1 Å, and ~4.3 Å) were used to generate a summed synthetic cryo-EM map using the same map parameters as the experimental EM density (see STAR Methods, Figure 8). The summed synthetic map was then used as input to the above-described pipeline, resulting in ten new models. This process was iterated five times, and the Cα RMSD of the resulting atomic models calculated at each iteration. These iterative refinements show that neither the mean Cα RMSD nor the

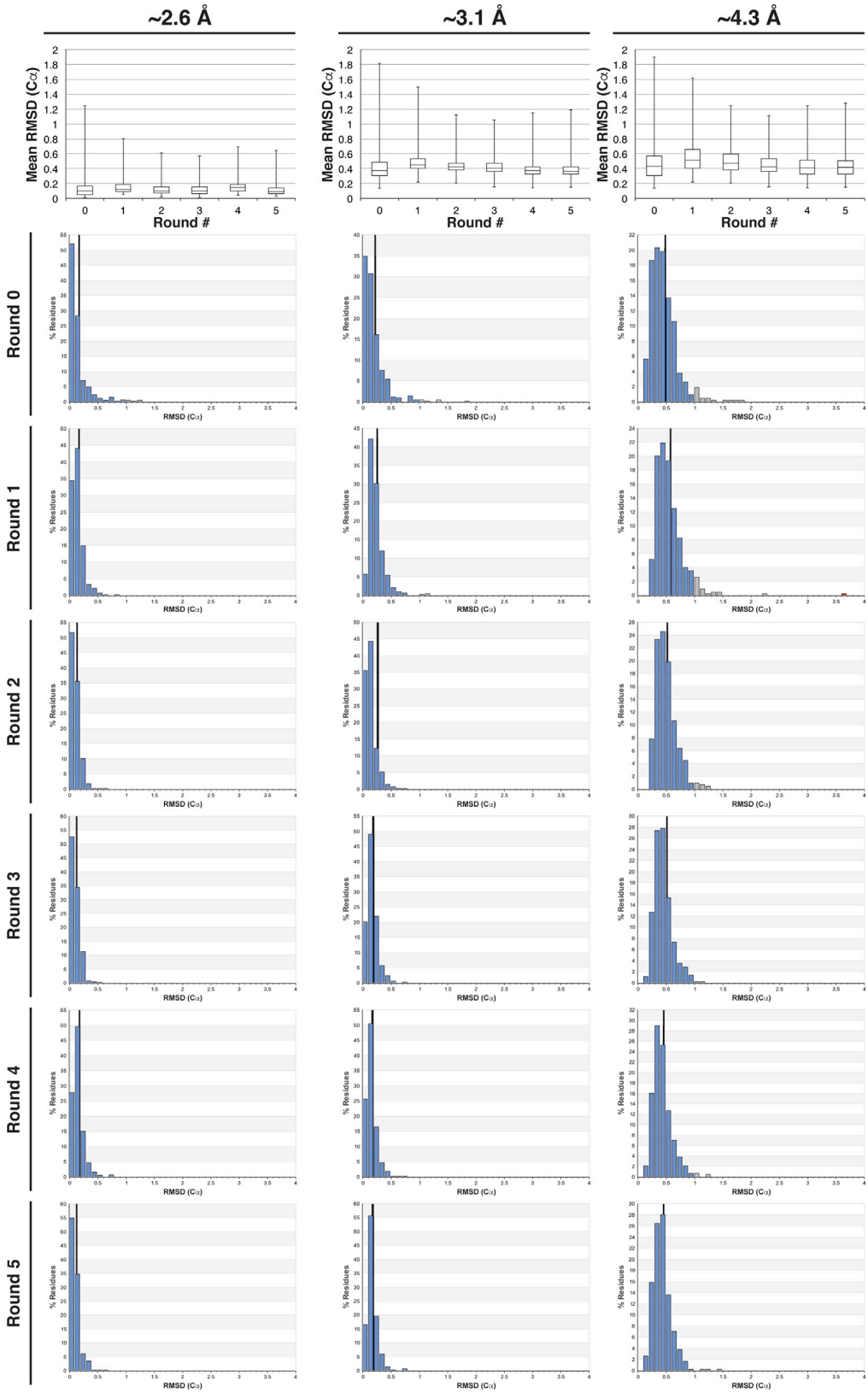

(legend on next page)

Cα RMSD histograms change substantially at a given resolution, indicating that the multiple models effectively regenerate the quality of the original cryo-EM map.

DISCUSSION

Here, we present a straightforward methodology to generate multiple independent models, each of which represent an approximately equally valid interpretation of the EM density. As the resolution of the target map worsens, and the extent of resolvable side chain densities decreases, the agreement in atomic coordinates across the multiple models decreases accordingly, with lower resolution structures exhibiting higher mean and per-residue RMSDs (Figure 1, Data S4). Importantly, this correlation is not limited solely to global map quality, i.e., nominal FSC-reported resolution, as the per-residue RMSD values correlate well to local resolution estimates. As such, maps exhibiting large variations in local resolution also exhibit large variances in per-residue RMSD values, with the least resolved regions of the maps also exhibiting the highest per-residue RMSD values (Figure 4).

We expect that an important use of the multiple models generated using these methodologies will be to define the range of structures that are compatible given the EM density. Because each model is generated using essentially the same calculation, the differences between the multiple models reflect the reproducibility of the refinement methodologies given the data, and provide a lower limit of the uncertainties of the structure calculation (Terwilliger et al., 2007). The uncertainty of the model coordinates provides a lower bound as to the precision of the models, informing on both map and model quality (de Bakker et al., 2006; DePristo et al., 2004; Ondracek and Mesters, 2006; Terwilliger et al., 2007). Comparison of the atomic coordinates across the ensemble is more informative and provides a better platform for drawing conclusions, minimizing the risk of structural overinterpretation resulting from the seemingly rigid single-structure models. Importantly, as has been discussed previously for ensembles refined against X-ray diffraction data, the PDB is amenable to deposition of multiple models and has tools in place for handling and annotating multi-model entries (response associated with Furnham et al. (2006)).

Visual examination of multiple models provides an immediate qualitative metric to even the most naive user. Specifically, the general user typically evaluates the ''correctness'' of an atomic model using a variety of metrics, including global model statistics (i.e., MolProbity score [Chen et al., 2010], map correlation coefficient, map-to-model FSC [DiMaio et al., 2013], Ramachandran outliers, EMRinger score [Barad et al., 2015], etc.), in addition to local examination of the model using B-factor analysis and fit to density. However, as described through our examination of EMD-3295, evaluating the ''correctness'' of an atomic model using B-factor analysis can be misleading about the extent of conformational heterogeneity present in the map. In the absence of the corresponding EM density, conventional models cannot always inform the general user of areas of poor model/map quality and/or poor model/map agreement. In contrast, evaluation of the multiple independent atomic models, even in the absence of the corresponding EM density, immediately provides a qualitative metric as to the ''correctness'' of the atomic coordinates, where regions or poor map quality will exhibit a large degree of heterogeneity in the atomic coordinates of the ensemble due to an inability of the refinement to converge to a single solution.

Compared with simulated data, the macromolecular structures deposited to the EMDB show a much higher degree of variability in the relationship between model convergence and reported global resolution. While non-linear regression analysis of *in silico* datasets and the previously deposited EMDB entries possess the same shape exhibited by the *in silico* datasets, the mean RMSD values for the EMDB entries are, on average, ~1 Å higher than the *in silico* datasets. This is not entirely unexpected, as the *in silico* datasets represent a best-case modeling scenario, with very stable and isotropically resolved maps, and the initial model derived from a high-resolution X-ray crystal structure. However, this disparity between the *in silico* datasets and the EMDB may be lessened with improvements in refinement algorithms, improvement in the accuracy of atomic electron scattering coefficients used during refinement, as well as more robust methods for identification of modeling errors.

These results represent an attempt to depart from the limitations of ascribing a map ''quality'' metric that is solely dependent on FSC. Beyond this study, we postulate several important developments to the multi-model approach will make this analysis more robust, including methodologies to apply these analyses to datasets that benefit from the combination of multiple EM maps (i.e., focused classification and/or refinements, regions that benefit from different sharpening values, etc.), or methodologies to assess which minimal combination of the best-scoring models best represent the data. These improvements in creating ensembles of independent models will address the issue of how *precisely* cryo-EM data can be represented by an individual model. However, as in high-resolution crystallography (Lang et al., 2010; Smith et al., 1986), we anticipate there will be cases where simple model types will not suffice as accurate descriptions of discrete conformational heterogeneity. Time-averaged ensembles (Burnley et al., 2012; Singharoy et al., 2016) and multi-conformer models (Keedy et al., 2015a) represent two possible paths toward modeling the alternative conformations that underlie the spatially distinct, yet ensemble-averaged, density. While the analysis of patterns of clashes (van den Bedem et al., 2013), time-resolved conformational changes (Cho et al., 2010; Hekstra et al., 2016), or temperature responses (Keedy et al., 2015b; Schmidt et al., 2013) can be used to infer the coupling between different conformationally heterogeneous degrees of freedom, there is no direct route to deriving and validating this information from a single X-ray diffraction experiment. In contrast,

Figure 8. Nested Refinements for 20S Proteasome Maps at ~2.6, ~3.1, and ~4.3 Å Resolution

For each 20S EM density, the top 10 scoring models (round 0) were used to generate a summed synthetic cryo-EM density. This synthetic EM density was then used as the input for the multi-model pipeline using the same initial model as the original survey, resulting in ten new models (round 1). This process was iterated four additional times (round 2–5) and the model-model convergence statistics were calculated for each round.

the single-particle nature of cryo-EM allows for focused reclassification to resolve the ensemble averaging of conformational heterogeneity into representative conformational states, and therefore the degree of long-range conformational coupling, across the entire macromolecule (Dashti et al., 2014; des Georges et al., 2016; Fernandez-Leiro and Scheres, 2016). The limits of these approaches have not yet been identified, but it is reasonable to expect that they will progress to routine reclassification of rigid body motions of subdomains (Maji et al., 2017) and perhaps secondary structures or even rotamers in the near future as instrumentation, data collection strategies, and processing algorithms improve. Evaluation of synthetic datasets, as used here to assess precision in modeling, will become increasingly important as the physical limits of reclassification are approached and the focus turns to validation and avoiding model bias.

STAR★METHODS

Detailed methods are provided in the online version of this paper and include the following:

- KEY RESOURCES TABLE
- CONTACT FOR REAGENTS AND RESOURCE SHARING
- METHOD DETAILS
  - 20S Proteasome Processing
  - β-Galactosidase Processing
  - Lower Resolution EM Density Generation
  - Multi-model Pipeline
  - Simulated EM Density Serial Refinements
  - Local Resolution Estimation and Display
- QUANTIFICATION AND STATISTICAL ANALYSIS
- DATA AND SOFTWARE AVAILABILITY

SUPPLEMENTAL INFORMATION

Supplemental Information includes three figures and four data files and can be found with this article online at https://doi.org/10.1016/j.str.2018.10.003.

ACKNOWLEDGMENTS

We thank Jean-Christophe Ducom at Scripps Research High Performance Computing for computational support, and Yiru Xu for help performing preliminary analyses of low-resolution densities for the "resolution devolution." We also thank members of the Lander lab and Elizabeth Villa for critical discussion of the manuscript. M.A.H. is supported by a Helen Hay Whitney Foundation postdoctoral fellowship. J.S.F is supported as a Searle Scholar, a Pew Scholar, a Packard Fellow, and by the National Science Foundation (STC-1231306) and the National Institutes of Health (GM063210). G.C.L. is supported as a Searle Scholar, a Pew Scholar, an Amgen Young Investigator, and by the National Institutes of Health (DP2EB020402). Computational analyses were performed using shared instrumentation funded by 1-S1OD021634 to G.C.L.

AUTHOR CONTRIBUTIONS

Conceptualization, Methodology, and Investigation: M.A.H. and G.C.L.; Formal Analysis: M.A.H., J.S.F., and G.C.L.; Visualization, Writing – Original Draft: M.A.H. and G.C.L.; Writing – Review & Editing: M.A.H., J.S.F., and G.C.L.

DECLARATION OF INTERESTS

The authors declare no competing interests.

Received: July 13, 2018
Revised: August 17, 2018
Accepted: October 10, 2018
Published: November 15, 2018

REFERENCES

Abeyrathne, P.D., Koh, C.S., Grant, T., Grigorieff, N., and Korostelev, A.A. (2016). Ensemble cryo-EM uncovers inchworm-like translocation of a viral IRES through the ribosome. Elife *5*, https://doi.org/10.7554/eLife.14874.

Adams, P.D., Afonine, P.V., Bunkoczi, G., Chen, V.B., Davis, I.W., Echols, N., Headd, J.J., Hung, L.W., Kapral, G.J., Grosse-Kunstleve, R.W., et al. (2010). PHENIX: a comprehensive Python-based system for macromolecular structure solution. Acta Crystallogr. D Biol. Crystallogr. *66*, 213–221.

Alberts, B. (1998). The cell as a collection of protein machines: preparing the next generation of molecular biologists. Cell *92*, 291–294.

Bai, X.C., Rajendra, E., Yang, G., Shi, Y., and Scheres, S.H. (2015). Sampling the conformational space of the catalytic subunit of human gamma-secretase. Elife *4*, e11182.

Banerjee, S., Bartesaghi, A., Merk, A., Rao, P., Bulfer, S.L., Yan, Y., Green, N., Mroczkowski, B., Neitz, R.J., Wipf, P., et al. (2016). 2.3 A resolution cryo-EM structure of human p97 and mechanism of allosteric inhibition. Science *351*, 871–875.

Barad, B.A., Echols, N., Wang, R.Y., Cheng, Y., DiMaio, F., Adams, P.D., and Fraser, J.S. (2015). EMRinger: side chain-directed model and map validation for 3D cryo-electron microscopy. Nat. Methods *12*, 943–946.

Bartesaghi, A., Matthies, D., Banerjee, S., Merk, A., and Subramaniam, S. (2014). Structure of beta-galactosidase at 3.2-A resolution obtained by cryo-electron microscopy. Proc. Natl. Acad. Sci. U S A *111*, 11709–11714.

Bartesaghi, A., Merk, A., Banerjee, S., Matthies, D., Wu, X., Milne, J.L., and Subramaniam, S. (2015). 2.2 A resolution cryo-EM structure of beta-galactosidase in complex with a cell-permeant inhibitor. Science *348*, 1147–1151.

Beadell, J.S., and Clark, D.S. (2001). Probing stability-activity relationships in the thermophilic proteasome from Thermoplasma acidophilum by random mutagenesis. Extremophiles *5*, 3–10.

Berman, H.M., Westbrook, J., Feng, Z., Gilliland, G., Bhat, T.N., Weissig, H., Shindyalov, I.N., and Bourne, P.E. (2000). The protein data bank. Nucleic Acids Res. *28*, 235–242.

Brown, A., Long, F., Nicholls, R.A., Toots, J., Emsley, P., and Murshudov, G. (2015). Tools for macromolecular model building and refinement into electron cryo-microscopy reconstructions. Acta Crystallogr. D Biol. Crystallogr. *71*, 136–153.

Burnley, B.T., Afonine, P.V., Adams, P.D., and Gros, P. (2012). Modelling dynamics in protein crystal structures by ensemble refinement. Elife *1*, e00311.

Campbell, M.G., Veesler, D., Cheng, A., Potter, C.S., and Carragher, B. (2015). 2.8 Å resolution reconstruction of the Thermoplasma acidophilum 20S proteasome using cryo-electron microscopy. Elife *4*, https://doi.org/10.7554/eLife.06380.

Cardone, G., Heymann, J.B., and Steven, A.C. (2013). One number does not fit all: mapping local variations in resolution in cryo-EM reconstructions. J. Struct. Biol. *184*, 226–236.

Chen, S., McMullan, G., Faruqi, A.R., Murshudov, G.N., Short, J.M., Scheres, S.H., and Henderson, R. (2013). High-resolution noise substitution to measure overfitting and validate resolution in 3D structure determination by single particle electron cryomicroscopy. Ultramicroscopy *135*, 24–35.

Chen, V.B., Arendall, W.B., 3rd, Headd, J.J., Keedy, D.A., Immormino, R.M., Kapral, G.J., Murray, L.W., Richardson, J.S., and Richardson, D.C. (2010). MolProbity: all-atom structure validation for macromolecular crystallography. Acta Crystallogr. D Biol. Crystallogr. *66*, 12–21.

Cho, H.S., Dashdorj, N., Schotte, F., Graber, T., Henning, R., and Anfinrud, P. (2010). Protein structural dynamics in solution unveiled via 100-ps time-resolved x-ray scattering. Proc. Natl. Acad. Sci. U S A *107*, 7281–7286.

Chowdhury, S., Carter, J., Rollins, M.F., Golden, S.M., Jackson, R.N., Hoffmann, C., Nosaka, L., Bondy-Denomy, J., Maxwell, K.L., Davidson,

A.R., et al. (2017). Structure reveals mechanisms of viral suppressors that intercept a CRISPR RNA-guided surveillance complex. Cell *169*, 47–57.e11.

Dambacher, C.M., Worden, E.J., Herzik, M.A., Martin, A., and Lander, G.C. (2016). Atomic structure of the 26S proteasome lid reveals the mechanism of deubiquitinase inhibition. Elife *5*, e13027.

Dashti, A., Schwander, P., Langlois, R., Fung, R., Li, W., Hosseinizadeh, A., Liao, H.Y., Pallesen, J., Sharma, G., Stupina, V.A., et al. (2014). Trajectories of the ribosome as a Brownian nanomachine. Proc. Natl. Acad. Sci. U S A *111*, 17492–17497.

Davis, J.H., Tan, Y.Z., Carragher, B., Potter, C.S., Lyumkis, D., and Williamson, J.R. (2016). Modular assembly of the bacterial large ribosomal subunit. Cell *167*, 1610–1622.e15.

de Bakker, P.I., Furnham, N., Blundell, T.L., and DePristo, M.A. (2006). Conformer generation under restraints. Curr. Opin. Struct. Biol. *16*, 160–165.

DePristo, M.A., de Bakker, P.I., and Blundell, T.L. (2004). Heterogeneity and inaccuracy in protein structures solved by X-ray crystallography. Structure *12*, 831–838.

des Georges, A., Clarke, O.B., Zalk, R., Yuan, Q., Condon, K.J., Grassucci, R.A., Hendrickson, W.A., Marks, A.R., and Frank, J. (2016). Structural basis for gating and activation of RyR1. Cell *167*, 145–157.e17.

DiMaio, F., Zhang, J., Chiu, W., and Baker, D. (2013). Cryo-EM model validation using independent map reconstructions. Protein Sci. *22*, 865–868.

Emsley, P., Lohkamp, B., Scott, W.G., and Cowtan, K. (2010). Features and development of Coot. Acta Crystallogr. D Biol. Crystallogr. *66*, 486–501.

Fernandez-Leiro, R., and Scheres, S.H. (2016). Unravelling biological macromolecules with cryo-electron microscopy. Nature *537*, 339–346.

Forster, A., Masters, E.I., Whitby, F.G., Robinson, H., and Hill, C.P. (2005). The 1.9 A structure of a proteasome-11S activator complex and implications for proteasome-PAN/PA700 interactions. Mol. Cell *18*, 589–599.

Frauenfelder, H., Sligar, S.G., and Wolynes, P.G. (1991). The energy landscapes and motions of proteins. Science *254*, 1598–1603.

Furnham, N., Blundell, T.L., DePristo, M.A., and Terwilliger, T.C. (2006). Is one solution good enough? Nat. Struct. Mol. Biol. *13*, 184–185, discussion 185.

Ge, J., Li, W., Zhao, Q., Li, N., Chen, M., Zhi, P., Li, R., Gao, N., Xiao, B., and Yang, M. (2015). Architecture of the mammalian mechanosensitive Piezo1 channel. Nature *527*, 64–69.

Goddard, T.D., Huang, C.C., and Ferrin, T.E. (2007). Visualizing density maps with UCSF Chimera. J. Struct. Biol. *157*, 281–287.

Goh, B.C., Hadden, J.A., Bernardi, R.C., Singharoy, A., McGreevy, R., Rudack, T., Cassidy, C.K., and Schulten, K. (2016). Computational methodologies for real-space structural refinement of large macromolecular complexes. Annu. Rev. Biophys. *45*, 253–278.

He, Y., Yan, C., Fang, J., Inouye, C., Tjian, R., Ivanov, I., and Nogales, E. (2016). Near-atomic resolution visualization of human transcription promoter opening. Nature *533*, 359–365.

Hekstra, D.R., White, K.I., Socolich, M.A., Henning, R.W., Srajer, V., and Ranganathan, R. (2016). Electric-field-stimulated protein mechanics. Nature *540*, 400–405.

Henderson, R., Sali, A., Baker, M.L., Carragher, B., Devkota, B., Downing, K.H., Egelman, E.H., Feng, Z., Frank, J., Grigorieff, N., et al. (2012). Outcome of the first electron microscopy validation task force meeting. Structure *20*, 205–214.

Heymann, J.B., and Belnap, D.M. (2007). Bsoft: image processing and molecular modeling for electron microscopy. J. Struct. Biol. *157*, 3–18.

Hryc, C.F., Chen, D.H., and Chiu, W. (2011). Near-atomic-resolution cryo-EM for molecular virology. Curr. Opin. Virol. *1*, 110–117.

Iudin, A., Korir, P.K., Salavert-Torres, J., Kleywegt, G.J., and Patwardhan, A. (2016). EMPIAR: a public archive for raw electron microscopy image data. Nat. Methods *13*, 387–388.

Joseph, A.P., Malhotra, S., Burnley, T., Wood, C., Clare, D.K., Winn, M., and Topf, M. (2016). Refinement of atomic models in high resolution EM reconstructions using Flex-EM and local assessment. Methods *100*, 42–49.

Juers, D.H., Jacobson, R.H., Wigley, D., Zhang, X.J., Huber, R.E., Tronrud, D.E., and Matthews, B.W. (2000). High resolution refinement of beta-galactosidase in a new crystal form reveals multiple metal-binding sites and provides a structural basis for alpha-complementation. Protein Sci. *9*, 1685–1699.

Keedy, D.A., Fraser, J.S., and van den Bedem, H. (2015a). Exposing hidden alternative backbone conformations in X-ray crystallography using qFit. PLoS Comput. Biol. *11*, e1004507.

Keedy, D.A., Kenner, L.R., Warkentin, M., Woldeyes, R.A., Hopkins, J.B., Thompson, M.C., Brewster, A.S., Van Benschoten, A.H., Baxter, E.L., Uervirojnangkoorn, M., et al. (2015b). Mapping the conformational landscape of a dynamic enzyme by multitemperature and XFEL crystallography. Elife *4*, e07574.

Kuriyan, J., Petsko, G.A., Levy, R.M., and Karplus, M. (1986). Effect of anisotropy and anharmonicity on protein crystallographic refinement. An evaluation by molecular dynamics. J. Mol. Biol. *190*, 227–254.

Kuzmanic, A., Pannu, N.S., and Zagrovic, B. (2014). X-ray refinement significantly underestimates the level of microscopic heterogeneity in biomolecular crystals. Nat. Commun. *5*, 3220.

Lander, G.C., Martin, A., and Nogales, E. (2013). The proteasome under the microscope: the regulatory particle in focus. Curr. Opin. Struct. Biol. *23*, 243–251.

Lander, G.C., Stagg, S.M., Voss, N.R., Cheng, A., Fellmann, D., Pulokas, J., Yoshioka, C., Irving, C., Mulder, A., Lau, P.W., et al. (2009). Appion: an integrated, database-driven pipeline to facilitate EM image processing. J. Struct. Biol. *166*, 95–102.

Lang, P.T., Ng, H.L., Fraser, J.S., Corn, J.E., Echols, N., Sales, M., Holton, J.M., and Alber, T. (2010). Automated electron-density sampling reveals widespread conformational polymorphism in proteins. Protein Sci. *19*, 1420–1431.

Lange, O.F., Lakomek, N.A., Fares, C., Schroder, G.F., Walter, K.F., Becker, S., Meiler, J., Grubmuller, H., Griesinger, C., and de Groot, B.L. (2008). Recognition dynamics up to microseconds revealed from an RDC-derived ubiquitin ensemble in solution. Science *320*, 1471–1475.

Leschziner, A.E., and Nogales, E. (2007). Visualizing flexibility at molecular resolution: analysis of heterogeneity in single-particle electron microscopy reconstructions. Annu. Rev. Biophys. Biomol. Struct. *36*, 43–62.

Levin, E.J., Kondrashov, D.A., Wesenberg, G.E., and Phillips, G.N., Jr. (2007). Ensemble refinement of protein crystal structures: validation and application. Structure *15*, 1040–1052.

Li, X., Mooney, P., Zheng, S., Booth, C.R., Braunfeld, M.B., Gubbens, S., Agard, D.A., and Cheng, Y. (2013). Electron counting and beam-induced motion correction enable near-atomic-resolution single-particle cryo-EM. Nat. Methods *10*, 584–590.

Maji, S., Shahoei, R., Schulten, K., and Frank, J. (2017). Quantitative characterization of domain motions in molecular machines. J. Phys. Chem. B *121*, 3747–3756.

McCammon, J.A., Gelin, B.R., and Karplus, M. (1977). Dynamics of folded proteins. Nature *267*, 585–590.

Merk, A., Bartesaghi, A., Banerjee, S., Falconieri, V., Rao, P., Davis, M.I., Pragani, R., Boxer, M.B., Earl, L.A., Milne, J.L., et al. (2016). Breaking Cryo-EM resolution barriers to facilitate drug discovery. Cell *165*, 1698–1707.

Naydenova, K., and Russo, C.J. (2017). Measuring the effects of particle orientation to improve the efficiency of electron cryomicroscopy. Nat. Commun. *8*, 629.

Neumann, P., Dickmanns, A., and Ficner, R. (2018). Validating resolution revolution. Structure *26*, 785–795.e4.

Nogales, E., and Scheres, S.H. (2015). Cryo-EM: a unique tool for the visualization of macromolecular complexity. Mol. Cell *58*, 677–689.

Ogura, T., Iwasaki, K., and Sato, C. (2003). Topology representing network enables highly accurate classification of protein images taken by cryo electron-microscope without masking. J. Struct. Biol. *143*, 185–200.

Ondracek, J., and Mesters, J.R. (2006). An ensemble of crystallographic models enables the description of novel bromate-oxoanion species trapped within a protein crystal. Acta Crystallogr. D Biol. Crystallogr. *62*, 996–1001.

Penczek, P.A. (2002). Three-dimensional spectral signal-to-noise ratio for a class of reconstruction algorithms. J. Struct. Biol. *138*, 34–46.

Penczek, P.A. (2010). Resolution measures in molecular electron microscopy. Methods Enzymol. *482*, 73–100.

Rohou, A., and Grigorieff, N. (2015). CTFFIND4: fast and accurate defocus estimation from electron micrographs. J. Struct. Biol. *192*, 216–221.

Roseman, A.M. (2004). FindEM–a fast, efficient program for automatic selection of particles from electron micrographs. J. Struct. Biol. *145*, 91–99.

Rosenthal, P.B., and Henderson, R. (2003). Optimal determination of particle orientation, absolute hand, and contrast loss in single-particle electron cryomicroscopy. J. Mol. Biol. *333*, 721–745.

Saxton, W.O., and Baumeister, W. (1982). The correlation averaging of a regularly arranged bacterial cell envelope protein. J. Microsc. *127*, 127–138.

Scheres, S.H. (2012). RELION: implementation of a Bayesian approach to cryo-EM structure determination. J. Struct. Biol. *180*, 519–530.

Scheres, S.H. (2014). Beam-induced motion correction for sub-megadalton cryo-EM particles. Elife *3*, e03665.

Scheres, S.H., and Chen, S. (2012). Prevention of overfitting in cryo-EM structure determination. Nat. Methods *9*, 853–854.

Schmidt, M., Srajer, V., Henning, R., Ihee, H., Purwar, N., Tenboer, J., and Tripathi, S. (2013). Protein energy landscapes determined by five-dimensional crystallography. Acta Crystallogr. D Biol. Crystallogr. *69*, 2534–2542.

Shen, P.S., Park, J., Qin, Y., Li, X., Parsawar, K., Larson, M.H., Cox, J., Cheng, Y., Lambowitz, A.M., Weissman, J.S., et al. (2015). Protein synthesis. Rqc2p and 60S ribosomal subunits mediate mRNA-independent elongation of nascent chains. Science *347*, 75–78.

Sigworth, F.J. (2007). From cryo-EM, multiple protein structures in one shot. Nat. Methods *4*, 20–21.

Singharoy, A., Teo, I., McGreevy, R., Stone, J.E., Zhao, J., and Schulten, K. (2016). Molecular dynamics-based refinement and validation for sub-5 A cryo-electron microscopy maps. Elife *5*, e16105.

Smith, J.L., Hendrickson, W.A., Honzatko, R.B., and Sheriff, S. (1986). Structural heterogeneity in protein crystals. Biochemistry *25*, 5018–5027.

Smock, R.G., and Gierasch, L.M. (2009). Sending signals dynamically. Science *324*, 198–203.

Subramaniam, S., Earl, L.A., Falconieri, V., Milne, J.L., and Egelman, E.H. (2016). Resolution advances in cryo-EM enable application to drug discovery. Curr. Opin. Struct. Biol. *41*, 194–202.

Tan, Y.Z., Baldwin, P.R., Davis, J.H., Williamson, J.R., Potter, C.S., Carragher, B., and Lyumkis, D. (2017). Addressing preferred specimen orientation in single-particle cryo-EM through tilting. Nat. Methods *14*, 793–796.

Tang, G., Peng, L., Baldwin, P.R., Mann, D.S., Jiang, W., Rees, I., and Ludtke, S.J. (2007). EMAN2: an extensible image processing suite for electron microscopy. J Struct. Biol. *157*, 38–46.

Terwilliger, T.C., Grosse-Kunstleve, R.W., Afonine, P.V., Adams, P.D., Moriarty, N.W., Zwart, P., Read, R.J., Turk, D., and Hung, L.W. (2007). Interpretation of ensembles created by multiple iterative rebuilding of macromolecular models. Acta Crystallogr. D Biol. Crystallogr. *63*, 597–610.

Tsai, K.L., Yu, X., Gopalan, S., Chao, T.C., Zhang, Y., Florens, L., Washburn, M.P., Murakami, K., Conaway, R.C., Conaway, J.W., et al. (2017). Mediator structure and rearrangements required for holoenzyme formation. Nature *544*, 196–201.

Urnavicius, L., Zhang, K., Diamant, A.G., Motz, C., Schlager, M.A., Yu, M., Patel, N.A., Robinson, C.V., and Carter, A.P. (2015). The structure of the dynactin complex and its interaction with dynein. Science *347*, 1441–1446.

van den Bedem, H., Bhabha, G., Yang, K., Wright, P.E., and Fraser, J.S. (2013). Automated identification of functional dynamic contact networks from X-ray crystallography. Nat. Methods *10*, 896–902.

van Heel, M., and Harauz, G. (1986). Resolution criteria for three dimensional reconstruction. Optik *73*, 119–122.

Voss, N.R., Yoshioka, C.K., Radermacher, M., Potter, C.S., and Carragher, B. (2009). DoG Picker and TiltPicker: software tools to facilitate particle selection in single particle electron microscopy. J. Struct. Biol. *166*, 205–213.

Wang, R.Y., Kudryashev, M., Li, X., Egelman, E.H., Basler, M., Cheng, Y., Baker, D., and DiMaio, F. (2015). De novo protein structure determination from near-atomic-resolution cryo-EM maps. Nat. Methods *12*, 335–338.

Wang, R.Y., Song, Y., Barad, B.A., Cheng, Y., Fraser, J.S., and DiMaio, F. (2016). Automated structure refinement of macromolecular assemblies from cryo-EM maps using Rosetta. Elife *5*, e17219.

Woldeyes, R.A., Sivak, D.A., and Fraser, J.S. (2014). E pluribus unum, no more: from one crystal, many conformations. Curr. Opin. Struct. Biol. *28*, 56–62.

Wuthrich, K. (1990). Protein structure determination in solution by NMR spectroscopy. J. Biol. Chem. *265*, 22059–22062.

Zhou, A., Rohou, A., Schep, D.G., Bason, J.V., Montgomery, M.G., Walker, J.E., Grigorieff, N., and Rubinstein, J.L. (2015). Structure and conformational states of the bovine mitochondrial ATP synthase by cryo-EM. Elife *4*, e10180.

STAR★METHODS

KEY RESOURCES TABLE

REAGENT or RESOURCE	SOURCE	IDENTIFIER
Deposited Data		
Raw, electron micrographs, *Escherischia coli* β-galactosidase with cell-permeant inhibitor	Bartesaghi et al., 2015	EMPIAR-10061
Raw, electron micrographs, *Thermoplasma acidophilum* 20S 5.6835mmproteasome core	Campbell et al., 2015	EMPIAR-10025
Cryo-EM structure, *Escherischia coli* β-galactosidase with cell-permeant inhibitor	Bartesaghi et al., 2015	EMDB-2984
Cryo-EM structure, *Thermoplasma acidophilum* 20S proteasome core	Campbell et al., 2015	EMDB-6287
Software and Algorithms		
Appion	Lander et al., 2009	http://emg.nysbc.org/redmine/projects/appion/wiki/Appion_Home
BSOFT	Heymann and Belnap, 2007	https://lsbr.niams.nih.gov/bsoft/
CTFFind4	Rohou and Grigorieff, 2015	http://grigoriefflab.janelia.org/ctffind4
Difference of Gaussian (DoG) picker	Voss et al., 2009	http://emg.nysbc.org/redmine/projects/software/wiki/DoGpicker
EMAN2	Tang et al., 2007	http://blake.bcm.edu/emanwiki/EMAN2/
FindEM	Roseman, 2004	http://emg.nysbc.org/redmine/projects/software/wiki/FindEM
MolProbity	Chen et al., 2010	http://molprobity.biochem.duke.edu
Motioncorr	Li et al., 2013	http://cryoem.ucsf.edu/software/driftcorr.html
Multi-variate statistical analysis/Multi-reference alignment (MSA/MRA) implemented using IMAGIC	Ogura et al., 2003	https://www.imagescience.de/imagic.html
Phenix 1.11-2520	Adams et al., 2010	https://www.phenix-online.org
RELION v1.4	Scheres, 2012, Scheres, 2014	https://www2.mrc-lmb.cam.ac.uk/relion/index.php/Main_Page
Rosetta	Wang et al., 2016	https://www.rosettacommons.org/software
UCSF Chimera	Goddard et al., 2007	https://www.cgl.ucsf.edu/chimera/

CONTACT FOR REAGENTS AND RESOURCE SHARING

Further information and requests for resources should be directed to and will be fulfilled by the Lead Contact, Gabe Lander (glander@scripps.edu).

METHOD DETAILS

It is expected that, without implementation of external molecular dynamics (MD) force fields, modeling and refinement of structures into maps at 5 Å resolution or worse is ill advised (Goh et al., 2016). Cryo-EM maps resolved to worse than 5 Å resolution have been the targets of a multitude of MD-centric refinement packages, and numerous groups have recently proposed the implementation of MD methodologies to validate the accuracy of atomic models generated from EM maps (Joseph et al., 2016; Singharoy et al., 2016). However, since the majority of near-atomic resolution structures are being build de novo from the cryo-EM density using software such as COOT (Emsley et al., 2010) and refined using crystallographic packages that have been modified to work with cryo-EM densities (Adams et al., 2010; Brown et al., 2015; Wang et al., 2016), we set a lower boundary of 5 Å for the generation of our set of EM densities and convergence tests.

20S Proteasome Processing

Super-resolution 8k x 8k micrograph movies (196 total movies, EMPIAR entry 10025 (Campbell et al., 2015)) with a super-resolution pixel size of 0.655 Å were corrected for beam-induced motion using MotionCorr 2.0, a modified version of MotionCorr (Li et al., 2013), using a 3 frame running average window. The resulting motion-corrected, summed frames were used for CTF estimation using CTFFind4 (Rohou and Grigorieff, 2015). Any micrographs with a CTF confidence value below 0.95 were discarded. A difference of Gaussian (DoG) picker (Voss et al., 2009) was used to select particles from the first 10 micrographs to yield an initial dataset of 627 particles. These particles were binned by 4 (2.62 Å/pixel and a box size of 128 pixels) and subjected to reference-free 2D classification using a topology representing network analysis (Ogura et al., 2003) and multi-reference alignment in Appion (Lander et al., 2009). The best 4 classes representing approximately all views were then used as templates against the entire dataset using FindEM (Roseman, 2004) yielding 141,988 particles. 2x decimated particles (1.31 Å/pixel and a box size of 256 pixels) were then subjected to reference-free 2D-classification using RELION v1.4 (Scheres, 2012). Particles (114,457) from the best classes were then subjected to 3D auto-refinement (0.655 Å/pixel and a box size of 512 pixels) using EMD-6287 (Campbell et al., 2015) as an initial model (low-pass filtered to 60 Å) with D7 symmetry imposed. Subsequent movie-refinement (with a running average of 7 frames) was followed by particle polishing (using a standard deviation of 200 pixels on the inter-particle distance and a 3 frame B-factor running average (Scheres, 2014)). The shiny particles were refined and subjected to a no alignment clustering using a mask against the full particle. This mask was generated using a 10-Å low-pass filtered version of the reconstructed map with a three-pixel extension and a five-pixel wide cosine-shaped soft edge. The best class (94,794 particles) from the resulting 3 classes was further refined using the same mask. The final resolution was estimated to ~2.7 Å using a gold-standard FSC cutoff of 0.143 (Henderson et al., 2012; Rosenthal and Henderson, 2003; Scheres and Chen, 2012) after using phase-randomization to account for the convolution effects of a solvent mask on the FSC between the two independently refined half maps (Chen et al., 2013) (Data S1).

β-Galactosidase Processing

Super-resolution 8k x 8k micrograph movies (EMPIAR entry 10061 (Bartesaghi et al., 2015)) were downscaled 2x (yielding a final pixel size of 0.637 Å). Beam-induced motion correction and CTF estimation were performed as described for the 20S dataset. Any micrographs with a CTF confidence value below 0.95 were eliminated from further processing. DoG picker (Voss et al., 2009) was used to select particles from the first 100 micrographs to yield an initial dataset of 12,195 particles. The best 8 classes representing approximately all views were then used as templates against the entire dataset using FindEM (Roseman, 2004) yielding an initial data set of 140,393 particles. 4x downscaled particles (2.548 Å/pixel and a box size of 96 pixels) were then subjected to reference-free 2D-classification using RELION. 97,188 particles from the best classes were then subjected to 3D auto-refinement using EMD-2984 (Bartesaghi et al., 2015) low-pass filtered to 60 Å as an initial model, with D2 symmetry imposed during the refinement. Particles were then re-centered and re-extracted, and all subsequent calculations were performed without binning (0.637 Å/pixel and a box size of 384 pixels). Movie-refinement with a running average of 7 frames was followed by particle polishing using a standard deviation of 1000 pixels on the inter-particle distance and a 3 frame B-factor running average (Scheres, 2014). The shiny particles were refined and subjected to a no alignment clustering using a mask against the full particle. This mask was generated using a 15-Å low-pass filtered version of the reconstructed map with a three-pixel extension and a five-pixel wide cosine-shaped soft edge. The best class (71,379 particles) from the resulting 3 classes was further refined using the same mask. The final resolution was estimated to ~2.2 Å based on the gold-standard FSC 0.143 cutoff (Henderson et al., 2012; Scheres and Chen, 2012) (Data S1l).

Lower Resolution EM Density Generation

The following protocol was used to generate lower resolution structures (nominal FSC-reported value to ~5 Å in increments of ~0.2 Å) for both the 20S proteasome and β-galactosidase using particles from the refinements detailed above. For each structure, a separate RELION *.star* file was created (i.e. *20S_half1.star*) that contained the particles from each half map utilized during the gold-standard refinement that yielded the highest resolution structure. Each of the two star files was then back projected with each particle being subjected to a random translational offset (i.e. 0 - 3.1 sigma pixel error) using the *relion_reconstruct* command. For example, the following command was used to generate a half map of the 20S core particle with a translational offset of 1 sigma:

relion_reconstruct –i 20S_half1.star –o 20S_1sigma_half1_class001_unfil.mrc –angpix 0.655 –sym D7 –ctf true –j 16 –shift_error 1

After generating the two half volumes for a desired translation error, the post-processing function within RELION was then used to create a single volume that had been sharpened and low-pass filtered (FSC-weighted) based on the FSC curve between the two half maps. The amount of per-particle translational shifts was adjusted empirically to obtain to a reconstruction at the approximate desired resolution. In total, 15 structures of the 20S proteasome from ~2.7 Å to ~4.9 Å resolution and 14 structures of β-galactosidase from ~2.2 Å to ~4.9 Å resolution were generated. Initially, both translational and rotational offsets were applied to generate lower resolution structures, but the resulting densities showed severe anisotropic loss of resolution. Adding even a small angular offset of 0.1 sigma resulted in reconstructions showing a severe loss of density in the peripheral regions, with only a small region of the core exhibiting structural features that corresponded to the FSC-reported resolution. For this reason, only translational offsets were applied in generating the multi-resolution suites.

Supporting the reliability of our *in silico* reconstructions and the resulting non-linear regression fit, analysis of the outputs from the multi-model pipeline reveal that the Cα RMSD values for 20S proteasome and β-galactosidase EMDB entries (EMD-2984, -5623, -5995, -6219, and -6287) lie on the same trend line as the *in silico* datasets. Maps estimated to have similar resolutions (i.e. the deposited ~4.8 Å resolution 20S proteasome EMDB entry 6219 and the ~4.7 and ~4.9 resolution *in silico* 20S

proteasome maps) report Cα RMSD values within the standard error of the measurements (Figure 5). These comparisons not only verify that multi-model analyses can report on map quality but also corroborate the ability of the *in silico* suite of structures to recapitulate the features of cryo-EM structures at a range of resolutions.

Multi-model Pipeline

All Electron Microscopy Data Bank (EMDB, www.emdatabank.org) depositions generated using C- or D- symmetries (i.e. C1, C2, D7, etc., not icosahedral or helical symmetries) having a reported resolution better than 5 Å (FSC gold-standard) with an associated PDB were used in this study. Analyses were limited to structures exhibiting C- or D-symmetry (i.e. C1, C2, D7, etc., not helical or icosahedral). These structure types were excluded because, at the time this study was initiated, refinement of these structure types using the employed software (Rosetta and PHENIX) were not robust. Current releases of these software packages now accommodate these structure types, so that the implementation and analysis described below is more broadly applicable (Chowdhury et al., 2017). If the deposited model for a symmetrized map only contained a single ASU, symmetry mates of the ASU were generated for these analyses. All EM densities were used without further modification. Initial models were generated by stripping PDB files of all alternate conformations, non-protein ligands/cofactors, resetting all occupancies to 1, and setting the isotropic B-factor to the approximate mean value. For entry 6287, model generation was performed as described in Campbell et al. (2015) prior to analysis using the pipeline detailed herein. Each entry was then refined using Rosetta with a selected output of 100 models using weighting terms based on reported resolution. The reported symmetry imposed during map generation was using during refinement. The 10 Rosetta-refined models that consistently scored best in categories such as geometry outliers (%, lower better), Ramachandran outliers (%, lower better), MolProbity clashscore (Chen et al., 2010) (value, lower better), and Rosetta aggregate score (Wang et al., 2016) (value, lower better) were selected as the ''best'' models for real-space refinement using the Phenix suite (Adams et al., 2010) with NCS parameters determined by map symmetry. The reported resolution of the corresponding EM density was used for both refinement programs.

Simulated EM Density Serial Refinements

For the 20S proteasome ~2.6 Å EM density, each of the top 10 atomic models obtained from the multi-model pipeline were converted to EM density using the Phenix software package, while maintaining information out to the Nyquist frequency (1.13 Å). The voxel size of each simulated EM density (0.31 Å/pixel) was then scaled to the same voxel size as the reference volume from which the models were refined against (0.655 Å/pixel), all 10 volumes were summed into a single volume, and then normalized against the reference volume using EMAN. This summed volume was then used as the reference volume for the multi-model pipeline, using the same initial model and parameters as those used for the original ~2.6 Å EM density. The outputted top 10 atomic models were converted to a summed EM density and this process was iterated 4 additional times. These analyses were also applied to the ~3.1 Å and ~4.3 Å 20S simulated EM densities.

Local Resolution Estimation and Display

The 'blocres' function in the Bsoft package (Heymann and Belnap, 2007) was used to generate local resolution maps, based on the two half-volumes outputted from the RELION 3D auto-refinement. All display images were generated using UCSF Chimera (Goddard et al., 2007).

QUANTIFICATION AND STATISTICAL ANALYSIS

In order to quantify the variability in atomic coordinates we measure the per-residue root-mean-square-deviation (RMSD) using backbone Cα atoms (for proteins) or C3′-C4′ atoms (for nucleic-acids). For each EMDB entry, these values were calculated across an ensemble of 10 independently-generated atomic models. These analyses were applied to 338 entries publicly available at from the EMDB (See Method Details).

DATA AND SOFTWARE AVAILABILITY

The methodology outlined in this manuscript can be performed in an automated fashion, and the multiple models for every EMDB included in this study, as well as the per-residue analyses have been made available online (www.lander-lab.com/convergence). New depositions to the EMDB will be automatically downloaded and analyzed using the pipeline described here, and the results made available on the webserver. Furthermore, we have made the multi-resolution 20S and β-galactosidase density suites available for download at this site. Any future updates to the processing strategy for generating per-residue RMSDs will be announced on this website.

Structure, Volume *27*

Supplemental Information

A Multi-model Approach to Assessing Local and Global Cryo-EM Map Quality

Mark A. Herzik Jr., James S. Fraser, and Gabriel C. Lander

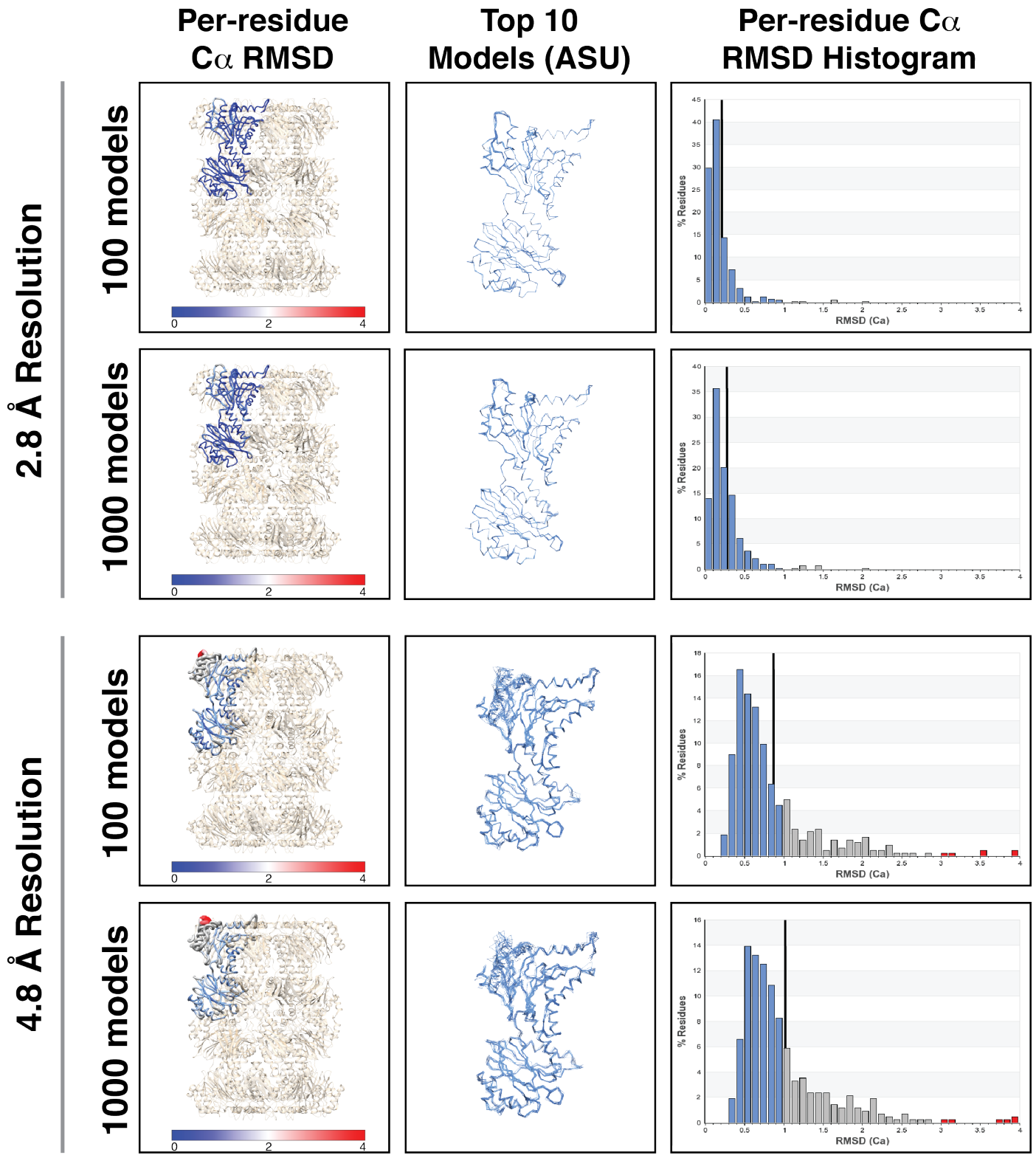

Figure S1, Related to Figure 1

Comparison of RMSD analyses starting with 100 or 1000 Rosetta models

The top 10 models from a set of 100 or 1000 Rosetta models were used to calculate the per-residue Cα RMSD statistics for the 20S proteasome at 2 resolutions. The worm representation (left panel), Cα overlay (middle panel), and RMSD histograms (right panel), do not show a notable difference in the results.

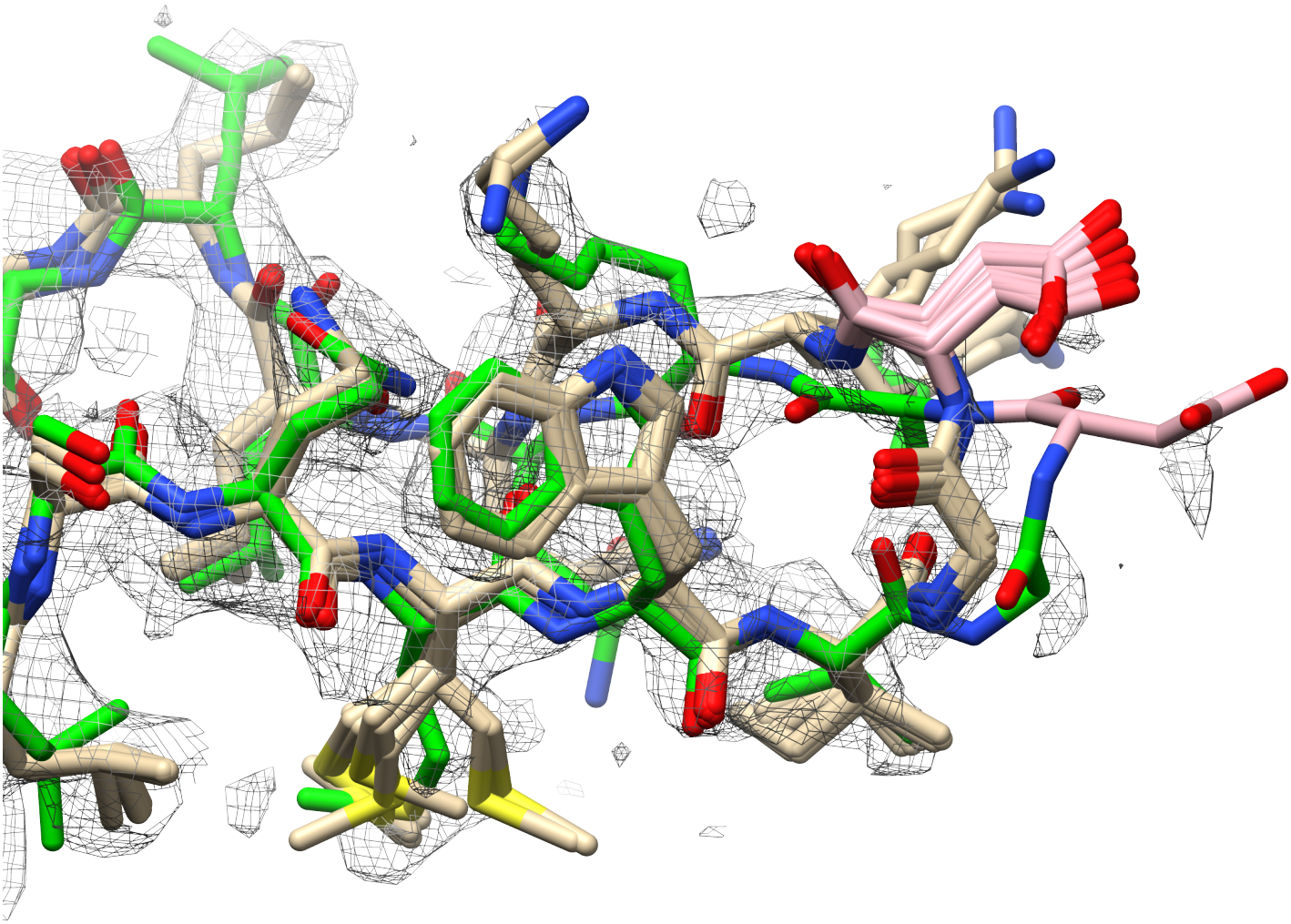

Figure S2, Related to Figure 2

Initial model errors removed through multi-model pipeline – case study EMD-2984

For models refined against EMDB-entry 2984, a loop comprising residues 766-778 is shown as sticks (green, PDB ID: 5A1A; wheat, top 10 models from multi-model pipeline). Aspartate 772 (shown in pink sticks) possesses a non-proline *cis* peptide bond in PDB ID: 5A1A (green) but adopts the *trans* configuration for all the top 10 models obtained via the multi-model pipeline (wheat).

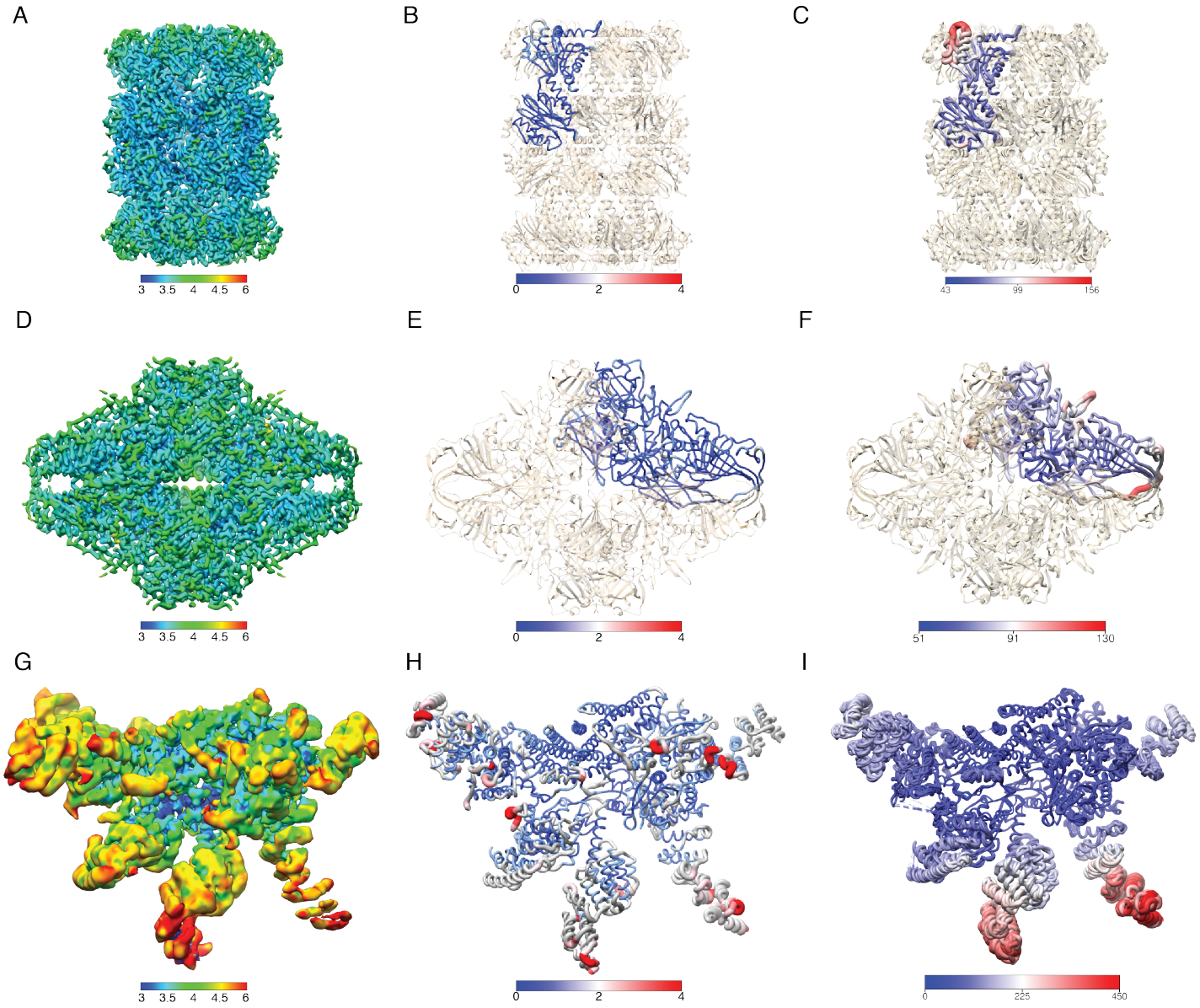

Figure S3, Related to Figure 4

EM density local resolution is correlated to per-residue Cα RMSD and B-factor

3D local resolution plots for cryoEM maps of 20S proteasome (panel A), β-galactosidase (panel D), and EMD-6479 (panel G) having overall FSC-reported resolutions of ~3.5 Å. Worm plots of the per-residue Cα RMSDs, (panels B, E, and H) and model B-factor (panels C, F, and I) are shown for each map. The worm plots show that areas exhibiting increased per-residue Cα RMSDs are correlated with lower local resolution estimates, as expected.